

ENVIRONMENTAL DEGRADATION OF CARBON-ALLOYED Fe_3Al -BASED INTERMETALLICS

by
MUKUT SEN



DEPARTMENT OF MATERIALS AND METALLURGICAL ENGINEERING
INDIAN INSTITUTE OF TECHNOLOGY KANPUR

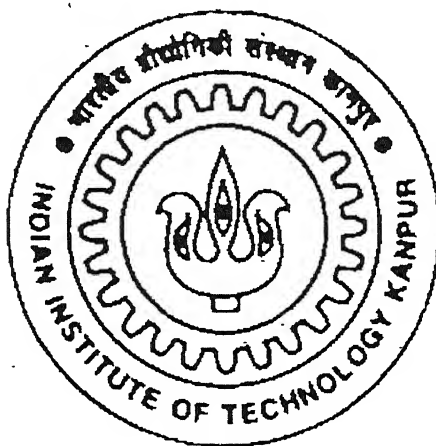
February, 2000

TH
MME/2000/M
855e

ENVIRONMENTAL DEGRADATION OF CARBON-ALLOYED Fe_3Al -BASED INTERMETALLICS

by

MUKUT SEN



DEPARTMENT OF MATERIALS AND METALLURGICAL ENGINEERING

INDIAN INSTITUTE OF TECHNOLOGY, KANPUR

FEBRUARY 2000

ENVIRONMENTAL DEGRADATION OF CARBON-ALLOYED Fe₃Al-BASED INTERMETALLICS

*A Thesis Submitted
in Partial Fulfilment of the Requirements
for the Degree of*

MASTER OF TECHNOLOGY

1289881

by

MUKUT SEN

to the

DEPARTMENT OF MATERIALS AND METALLURGICAL ENGINEERING

INDIAN INSTITUTE OF TECHNOLOGY, KANPUR

FEBRUARY 2000

15 MAY 2000 / MME

CENTRAL LIBRARY
I. I. T., KANPUR

A 130851

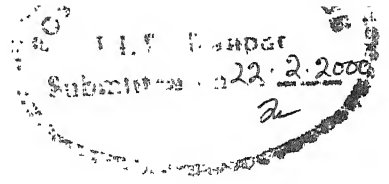
"4)

MME/PO/6/1

S 550



A130851



CERTIFICATE

This is to certify that the present work, entitled **ENVIRONMENTAL DEGRADATION OF CARBON-ALLOYED Fe₃Al-BASED INTERMETALLICS**, has been carried out by Mr. Mukut Sen under my supervision and to the best of my knowledge it has not been submitted elsewhere for a degree.

(Dr. R. BALASUBRAMANIAM)

Associate Professor

Department of Materials and Metallurgical Engineering
Indian Institute of Technology
Kanpur 208016, INDIA

Date: 26nd February 2000

Acknowledgement

I acknowledge with sincerity and deep sense of gratitude the expert guidance and continuous encouragement provided by my thesis supervisor Dr. R. Balasubramaniam throughout the course of this thesis.

I wish to express my sincere appreciation of valuable help and suggestions obtained from Dr. M. N. Mungole. Special thanks to him too for providing me with all possible helps regarding consumables, laboratory accessibility and technical knowhow.

I am thankful to Dr. A.V.Ramesh Kumar for his help regarding potentiodynamic experiment.

I am thankful to Mr. Umashankar, Mr. Jain and Mr. K. P. Mukherjee for their help and guidance during my experiments.

Thanks are due to all my friends from department and outside who have helped me in various capacities throughout my stay at Kanpur. Prominent amongst them are RP, Saumya, Palash, Ajay, Nikhil, Som, Pinaki, Srikanta, Ritwik, Sankha, Gautam, Badru, Ram.... The list goes on and is in no means exhaustive.

At the end I am thankful to all those who helped me directly or indirectly during my stay in IIT Kanpur.

Mukut Sen.

Contents

	Page Number
Abstract	i
List of Figures	iii
List of Tables	v
Chapter 1 Introduction	
1.1 Intermetallics	1
1.2 Iron Aluminides	2
1.3 Carbon-Alloyed Iron Aluminide	2
1.4 Objectives of the Present Study	3
1.5 Plan of Work	3
Chapter 2 Literature Review	
2.1 Phase Diagram and Structures	5
2.2 Room Temperature Mechanical Behavior	9
2.3 Hydrogen Embrittlement Mechanism	12
2.4 Hydrogen Diffusion in Iron Aluminide	16
2.5 Minimizing Hydrogen Embrittlement	19
2.5.1 Ductility Improvement by Alloying	19
2.5.2 Ductility Improvement by Thermomechanical Processing	22
2.5.3 Surface Modification	24
2.5.4 Ductility Improvement by Passivity Induction	26
2.5.5 Irreversible Hydrogen Trapping	28
Chapter 3 Experimental Procedure	
3.1 Materials	30
3.2 Polarization Studies	31
3.3 Hydrogen Diffusion Study	32

3.4	Microhardness	32
3.5	X-ray Diffraction	32
3.6	Immersion Testing	33
3.7	Mechanical Testing	33
3.8	Optical Microscopy	34
3.9	Scanning Electron Microscopy	34
3.10	EPMA Study	35
Chapter 4	Results and Discussions	
4.1	Microstructural Study	36
4.2	Composition Analysis	41
4.2.1	Electron Probe Microanalysis	41
4.2.2	X-ray Diffraction	41
4.3	Hydrogen Diffusivity	44
4.4	Room Temperature Aqueous Corrosion	48
4.4.1	Potentiodynamic Polarization	48
4.4.2	Corrosion Kinetics	53
4.5	Mechanical Properties	59
4.6	Fractography Study	62
4.7	Effect of Hydrogen Charging on Microstructure	65
Chapter 5	Summary and conclusions	
5.1	Conclusions	69
5.2	Suggestions for Future Work	71
References		72

Abstract

The effect of carbon addition to the iron aluminides on several properties was addressed in the study. These studies included microstructural, electrochemical and hydrogen embrittlement characterization. The iron aluminides used in the present study were obtained from the Defense Metallurgical Research Laboratory, Hyderabad and they possessed the composition (in atom percent) Fe-28Al-2.1C (referred as ESR56) and Fe-27.4Al-3.6C (referred as ESR63). They were processed electroslag remelting.

The salient conclusions of the present study are summarized. The microstructures of the carbon-alloyed iron aluminides confirmed the presence of Fe_3AlC precipitates. These precipitates were present in two shapes: spherical (which were relatively large) and needle-shaped (which were relatively small). The presence of this carbide was also validated by XRD study. The diffusivities of hydrogen in both the samples were determined by the technique of subscale microhardness profiling after cathodic hydrogen charging. The estimated hydrogen diffusivities (in m^2/s) were 9.33×10^{-15} for ESR56 and 8.62×10^{-15} for ESR63. The lower hydrogen diffusivity in ESR63 should be related to the larger volume fraction of carbides in the alloy. This indirectly indicated that carbide particles (Fe_3AlC) act as the irreversible hydrogen trapping sites and lower hydrogen diffusivity. The location where hydrogen is irreversibly trapped is not exactly known, but most likely at the carbide-metal interfaces.

Electrochemical polarization studies indicated that the alloys exhibit active-passive behaviour in acidic solution (0.05 mol/l H_2SO_4) whereas they exhibit stable passivity in pH=8.4 buffer solution (0.15N Boric acid + 0.15 N $\text{Na}_2\text{B}_4\text{O}_7 \cdot 10\text{H}_2\text{O}$). Corrosion kinetics was studied by weight loss method. In the long-term experiment of eight days, the corrosion rates were higher in after the first 12 hours for both the samples (ESR56 and ESR63). In the short-term experiment of 24 hours, the rate of corrosion was higher in the initial stages of experiment. The enhanced corrosion rates in the initial periods of immersion were due to the selective dissolution of the matrix. Once the equilibrium conditions were attained, the corrosion rate decreased. Microstructural observations

indicated that the carbide-matrix interfaces were severely corroded, which has been explained based on distance effect in galvanic corrosion.

As regards the mechanical properties in the presence of hydrogen, the specimens exhibited poor ductilities both in the uncharged and charged+baked conditions. The deterioration in mechanical properties on hydrogen charging was relatively more in the case of ESR63 compared to ESR56. This has been related to initiation of fracture at the carbide-matrix interfaces. Both the alloys exhibited brittle cleavage type fracture after hydrogen charging+baking. In cases where some ductility was observed, the fracture was mixed mode type. The effect of hydrogen charging on microstructure was also studied separately by scanning electron microscopy. Several carbide particles were cracked after charging and moreover, the presence of cracks in the carbides could be seen. There were several carbide particles where pores could be identified at the carbide-matrix interfaces. Finally, it was also observed that the matrix had corroded to some extent upon cathodic hydrogen charging. The cracking of the carbide precipitates on hydrogen charging could result either due to a chemical reaction of the carbide with hydrogen or due to lattice dilation caused by the solution of hydrogen. Based on the microstructural study, it is more likely that the deleterious effect of hydrogen charging+baking on the mechanical properties is related to the initiation of cracks at the regions, i.e. the carbide-matrix interfaces, where it locally accumulates.

List of Figures

	Page Number
1 The Fe-Al phase diagram	6
2 The DO ₃ and B2 ordered crystal structures of iron aluminides	7
3 Schematic tensile stress-strain behavior of iron aluminides in various environments at ambient temperature	11
4 Hydrogen entry into the material. Processes that occur at the crack tip during hydrogen embrittlement	13
5 Hydrogen embrittlement mechanism by the decohesion mechanism in iron aluminides	15
6 Diffusivity of hydrogen in α -Fe [8]	17
7 Arrhenius representation of diffusivity of hydrogen in α -Fe [23]	18
8 Optical microstructure of (a) as received ESR56 sample, and (b) as received ESR63 sample	38
9 SEM micrographs of (a) as received ESR56 sample, and (b) as received ESR63 sample	39
10 X-ray diffraction pattern of (a) ESR56 and (b) ESR 63 samples, using CuK α radiation ($\lambda=0.15405\text{nm}$)	42
11 Microhardness profile of ESR56, ESR63 and Fe-25Al intermetallics, along the thickness direction after cathodic hydrogen charging for 12 hours at 10 mA/cm ² in 0.05 mol/l H ₂ SO ₄ solution	46
12 Potentiodynamic polarization behavior of ESR56, ESR63 intermetallics along with Fe-28Al intermetallic in 0.05 mol/l H ₂ SO ₄ solution [38]	49
13 Potentiodynamic polarization behavior of ESR56 and ESR63 samples in buffer solution	50

14	Long term immersion testing of ESR56 and ESR63 samples	55
15	Short term immersion testing of ESR56 and ESR63 samples	56
16	SEM micrograph of (a) ESR56 alloy and (b) ESR63 alloy after immersion in 0.05 mol/l H ₂ SO ₄ solution for 2 hours.	57
17	SEM micrograph of (a) ESR56 alloy and (b) ESR63 alloy after immersion in 0.05 mol/l H ₂ SO ₄ solution for 24 hours.	58
18	SEM fractograph of tensile sample after hydrogen charging+ baking, showing interfaces are severely affected	61
19	SEM fractograph of tensile sample after hydrogen charging+ baking, (a) showing delamination effect at the carbide-matrix interfaces, and (b) showing mainly cleavage type of fracture surface	63
20	SEM fractograph of tensile sample with out hydrogen charging, (a) showing fracture mainly originated from the carbide-matrix interfaces, and (b) showing mixed mode (ductile-brittle) fracture surface	64
21	SEM micrographs of the carbon-alloyed intermetallic after hydrogen charging for 12 hours at 10 mA/cm ² in 0.05 mol/l H ₂ SO ₄ solution, showing (a) some cracked carbides particles, and (b) pore formation in the carbide particle	68

List of Tables

	Page Number
1 Typical room temperature properties of iron aluminide [3]	8
2 Typical room temperature properties of iron aluminides [3] after (a) heat treatment for 2 hour at 700°C (B2 structure), and (b) after heat treatment for 120 hour at 500°C (DO ₃ structure) [11]	10
3 Room temperature mechanical properties of Fe-28Al and Fe ₃ Al + Cr alloys	21
4 Effect of surface condition on room temperature properties of Fe-28Al [5]	25
5 Effect of surface metallic coatings on the room temperature mechanical properties of iron aluminides [38]	27
6 Size, volume fraction and surface area per unit volume of the spherical carbide particles distributed in ESR56 and ESR63 samples	40
7 Analysis of the X-ray diffractogram of ESR56 using CuK _α radiation ($\lambda = 0.15405$ nm)	43
8 Analysis of the X-ray diffractogram of ESR63 using CuK _α radiation ($\lambda = 0.15405$ nm)	43
9 Estimated diffusivity of hydrogen in the samples	47
10 Parameters determined from potentiodynamic polarization curves in buffer and 0.05 mol/l H ₂ SO ₄ solution for ESR56 and ESR63 samples	51
11 Corrosion rates of the samples at room temperature in 0.05 mol/l H ₂ SO ₄ solution	54
12 Room temperature mechanical properties of hydrogen-charged + baked and uncharged carbon-alloyed intermetallics	60

Chapter 1

INTRODUCTION

The topic of present study is *Environmental Degradation of Carbon-Alloyed Fe₃Al-based intermetallics*. This chapter introduces the subject of intermetallics, with emphasis on iron aluminides. The technical importance of this material has motivated investigation in this direction and towards understanding of the topic mentioned. The chapter concludes with the objective of the present study and the plan of work.

1.1 Intermetallics

Ordered intermetallics constitute an unique class of advanced materials that form long range-ordered crystal structure below a critical temperature termed as the critical ordering temperature (T_c) [1]. These usually exists in relatively narrow or fixed compositional ranges around simple stoichiometric ratios (similar to inorganic compounds). The need to develop materials possessing high specific strength for structural applications at elevated temperatures has motivated research in the area of ordered intermetallics.

Intermetallic aluminide posses many interesting features that project them as candidate material for high temperature structural applications [2]. They contain enough aluminium to form, in oxidizing environments, thin film of aluminium oxide that are often compact and protective. They are characterized by low densities, relatively high melting points and good mechanical properties at elevated temperatures. The aluminides that have attracted attention as potential candidates for high temperature applications include titanium, nickel and iron aluminides, and hence have undergone extensive development in the recent past, primarily for high temperature applications. Research on these materials are being conducted extensively for effecting modifications on the existing systems (either by alloying or by the modifications in the processing steps) in order to optimize their

properties. In the present thesis, effect of carbon addition in iron aluminide on mechanical and environmental degradation (hydrogen embrittlement and corrosion) behavior would be addressed specifically.

1.2 Iron Aluminides

Important iron aluminides are ordered intermetallics centered around the composition Fe_3Al and FeAl . These iron aluminides possess attractive properties for application at elevated temperatures and severe environments over conventional structural materials like stainless steel and nickel-based super alloys. Specific advantages include, excellent sulphidation resistance, very good oxidation resistance, lower density ($5400\text{-}6700\text{ kg/m}^3$) which is 30% of that of the commercially available high temperature materials, good wear resistance, good cavitation erosion resistance, potentially lower cost and reduced consumption of strategic element such as chromium [3]. One of the key factors in increasing the maximum use temperature is enhanced oxidation resistance.

The lack of ductility at room temperature limits use of these base iron aluminides as useful engineering materials. This has been well identified to be caused by an extrinsic effect, namely environmental embrittlement due to hydrogen [4]. Hydrogen is produced as a result of the reaction of the fresh surface of iron aluminide with moisture and therefore, the poor room temperature ductility has been attributed to moisture-induced embrittlement. Most of the methods proposed to tackle hydrogen embrittlement (HE) rely on restricting the entry of hydrogen into the lattice. This achieved either by thermo-mechanical treatments [5] or by surface modifications (directly by coatings [6] or indirectly by alloying with passivity inducing elements [7,8]). In addition, alloying could also be effective in enhancing other mechanical properties of the intermetallics. It has been proposed that alloying with passivity inducing elements in appropriate proportion (less than solubility limit) to iron aluminides would reduce the hydrogen liberation rates on the surface and passive layer would further hinder the diffusion of hydrogen into the intermetallic, thereby minimize HE [7]. In the present study, the carbon-alloyed iron aluminide is addressed with specific reference to possible minimization of HE.

1.3 Carbon Alloyed Iron Aluminide

Ordered intermetallic alloys based on the iron aluminide are being considered for high temperature structural applications. Though these alloys exhibit poor room temperature ductility and

low fracture toughness, significant improvement in these respects can be achieved by alloying addition and process control. Most of the literature is on iron aluminide compositions with very low (0.01 wt%) carbon contents because carbon is known to embrittle these alloys causing significant reduction in ductility. However, no reason has been ascribed to this loss in ductility. Recently Salazar *et al* have reported that addition of carbon in the range of 0.1 to 0.50 wt% significantly increases the room temperature strength of Fe-16 wt% (28 at%) Al alloys [9]. These alloys also exhibited good room temperature ductility, due to the entrapment of hydrogen by Fe₃AlC particles, which was proposed to lower hydrogen diffusivity in these alloys and reduce the susceptibility to environmental embrittlement [9]. The increase in room temperature yield strength was attributed to solid solution strengthening by the interstitial carbon, as well as precipitation hardening due to the presence of Fe₃AlC precipitates [13].

These carbon alloyed iron aluminides were produced in DMRL, Hyderabad by a combination of air induction melting and electroslag remelting (ESR). The melting practice has been described in detail in next chapter. The ESR ingots were held at 1000°C for 1 hour and hot forged in one tonne press with die platens at room temperature. The ESR ingots exhibited columnar grains having an average grain diameter of 1750 µm before forging. After forging, with reduction ratio of 70% exhibited recrystallized grains [9].

1.4 Objectives of the Present Study

The present study is specifically concerned with the room temperature properties of the carbon-alloyed iron aluminide. It is well known that the base iron aluminide has low room temperature ductility and this is attributed to the hydrogen embrittlement. As the carbon-alloyed iron aluminide contains Fe₃AlC precipitates, their effect on HE, corrosion behavior and mechanical properties are to be investigated. These are the main objectives of the study.

1.5 Plan of Work

The carbon alloyed iron aluminides have been developed in DMRL, Hyderabad by a combination of air induction and electroslag remelting (ESR). These ESR ingots were forged to a reduction ratio of 70% and showed recrystallized grains. Two kinds of samples were obtained with the major difference being the carbon content. The compositions (in atom percent) are Fe-28.1Al-2.1C and Fe-27.46Al-3.66C. The work planned schedule consisted of the following sequences:

- 1) Microstructural characterization of the samples by optical and scanning electron microscopy.
- 2) Determination of hydrogen diffusivity by subscale microhardness profiling.
- 3) Characterization of the materials by X-ray diffraction.
- 4) Mechanical behavior of tensile specimens as per ASTM standards to assess the HE nature.
- 5) Characterization of fracture surface by SEM.
- 6) Electrochemical characterization by potentiodynamic polarization study at room temperature.
- 7) Corrosion kinetics by immersion testing.
- 8) Effect of hydrogen charging on microstructure.

Chapter 2

Literature Review

The phase diagram and structure of iron aluminides would be briefly reviewed in the beginning of the chapter. The room temperature mechanical properties of iron aluminides would be addressed. The methods that have been utilized to provide enhanced ductility to iron aluminide would be discussed in detail. These methods include alloying, thermo-mechanical processing, surface modification and passivity induction. Specific attention would be focussed on the role of hydrogen in affecting the room temperature ductility, with special reference to hydrogen diffusivity in iron aluminides. The alloy development methodology to produced ductile iron aluminides currently being followed at IIT, Kanpur would be detailed in these discussions. Finally, the chapter ends with a brief survey of room temperature aqueous corrosion of iron aluminide.

2.1 Phase Diagram and Structures

Ordered iron aluminides exist in relatively narrow compositional ranges around simple stoichiometric ratios. The phase diagram of Fe-Al system is shown in Figure 1. Iron aluminides based on Fe_3Al and FeAl can exist in two crystal allotropic modifications. These structures (DO_3 and B2) are both ordered BCC structures and these are presented in Figure 2. Fe_3Al can exist both B2 and DO_3 ordered structure (depending upon the temperature) while FeAl can exist only in the B2 ordered form. Table 1 presents some typical room temperature properties and critical ordering temperatures for different allotropic modifications of iron aluminides [3]. The room temperature strength and room temperature ductility of the iron aluminides are low.

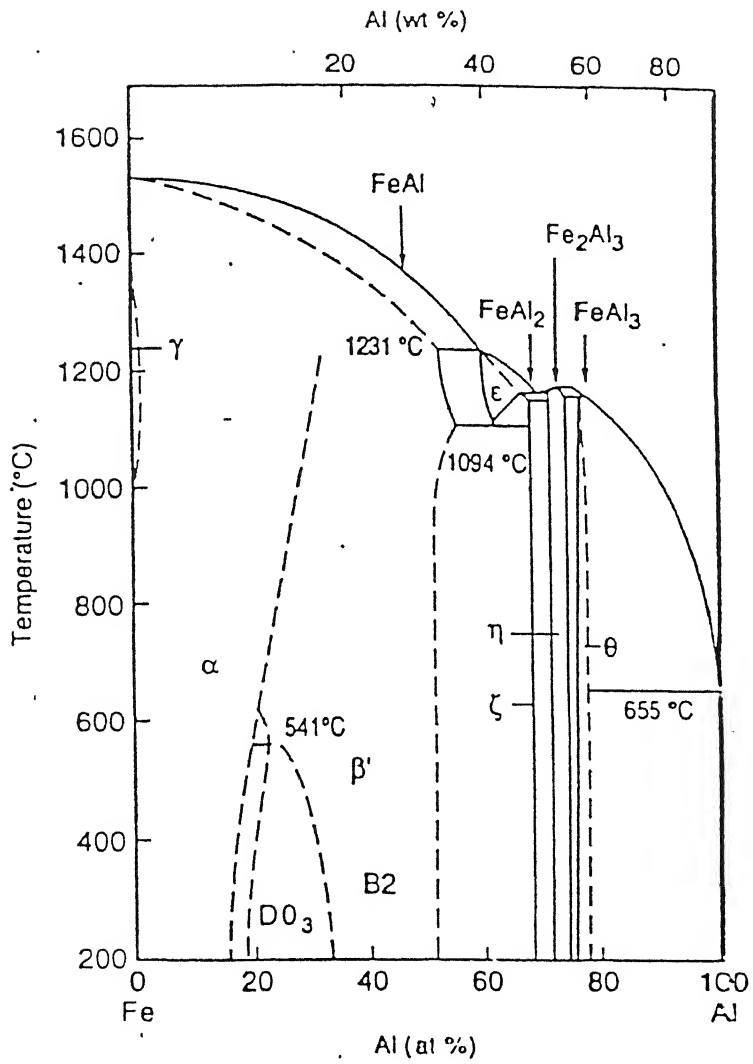


Figure 1 The Fe-Al phase diagram

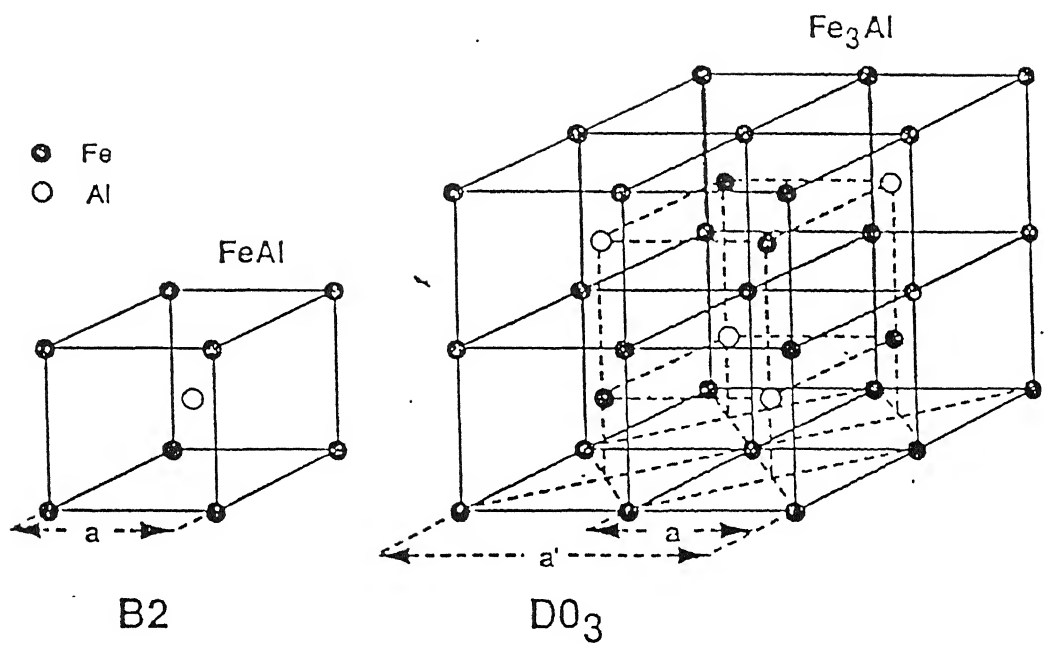


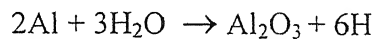
Figure 2 The DO₃ and B2 ordered crystal structure of iron aluminides

Table 1: Typical room temperature properties of iron aluminide [3]

Alloy	Crystal structure	Ordering temp.	Melting point	Density (gm/cc)	Y.S (MPa)	Elongation (%)
Fe ₃ Al	DO ₃	540°C	1540 °C	6.72	300	3.7
Fe ₃ Al	B2	760 °C	1540 °C	6.72	380	4.1
FeAl	B2	1250 °C	1250 °C	5.56	360	2.2

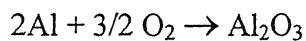
2.2 Room Temperature Mechanical Behavior

Iron aluminides have been known to be brittle at room temperature for more than 50 years since the first study conducted in 1930 [10]. However, the major cause of their low ductility and brittle fracture was not known. Recently, Liu *et al* have proposed an environmental effect as the major cause for room temperature embrittlement in iron aluminides [11]. They proposed that the embrittlement involves the reaction of water vapour with aluminium and the reaction product, atomic hydrogen \rightarrow enters the lattice and cause embrittlement.

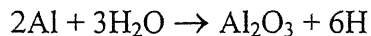


Direct evidence has also been provided recently for the production of hydrogen by reaction of iron aluminide with water vapour by Zhu *et al* [12] by a laser mass spectroscopic technique.

That hydrogen is the main damaging agent causing poor ductility was confirmed from tensile tests conducted in different environments. These results are summarized in Table 2. The effect of various test environments on the room temperature stress-strain behavior of iron aluminide is shown schematically in Figure 3. As evident from the figure ductility is higher in Ar+4% H_2 environment rather than humid air. This is because molecular hydrogen does not cause much embrittlement in Fe_3Al , because of its lower activity as compared with atomic hydrogen produced from water vapour reaction. As seen in this figure, testing in water vapour environment show the least ductility and vacuum/oxygen environments provide high ductility. Liu *et al* have shown that higher ductilities are observed in a dry oxygen environment rather than in vacuum because oxygen reacts with aluminium to form Al_2O_3 directly [11]



thereby suppressing the aluminium-moisture reaction which provides nascent hydrogen.



Generation of atomic hydrogen is suppressed and thus higher ductility is observed in dry oxygen environment.

Hence the most crucial factor in improving the room temperature mechanical properties of iron aluminides, i.e. the ductility, is to restrict the entry of hydrogen into the material. Now the following sub-sections review the methods employed by researchers in achieving the above goal.

\rightarrow
or paragraph

Table 2a : Room temperature tensile properties of iron aluminides after heat treatment for 2 hr at 700°C (B2 structure) [11]

Environment	Y.S.(MPa)	U.T.S.(MPa)	Ductility(%)
Vacuum	387	851	12.8
Oxygen	392	867	12.0
Air	387	559	4.1
H ₂ O vapour	387	475	2.1

Table 2b : Room temperature tensile properties of iron aluminides after heat for 120 hr at 500°C (DO₃ structure) [11]

Environment	Y.S.(MPa)	U.T.S.(MPa)	Ductility(%)
Vacuum	316	813	12.4
Oxygen	298	888	11.7
Air	279	514	3.7
H ₂ O vapour	322	439	2.1

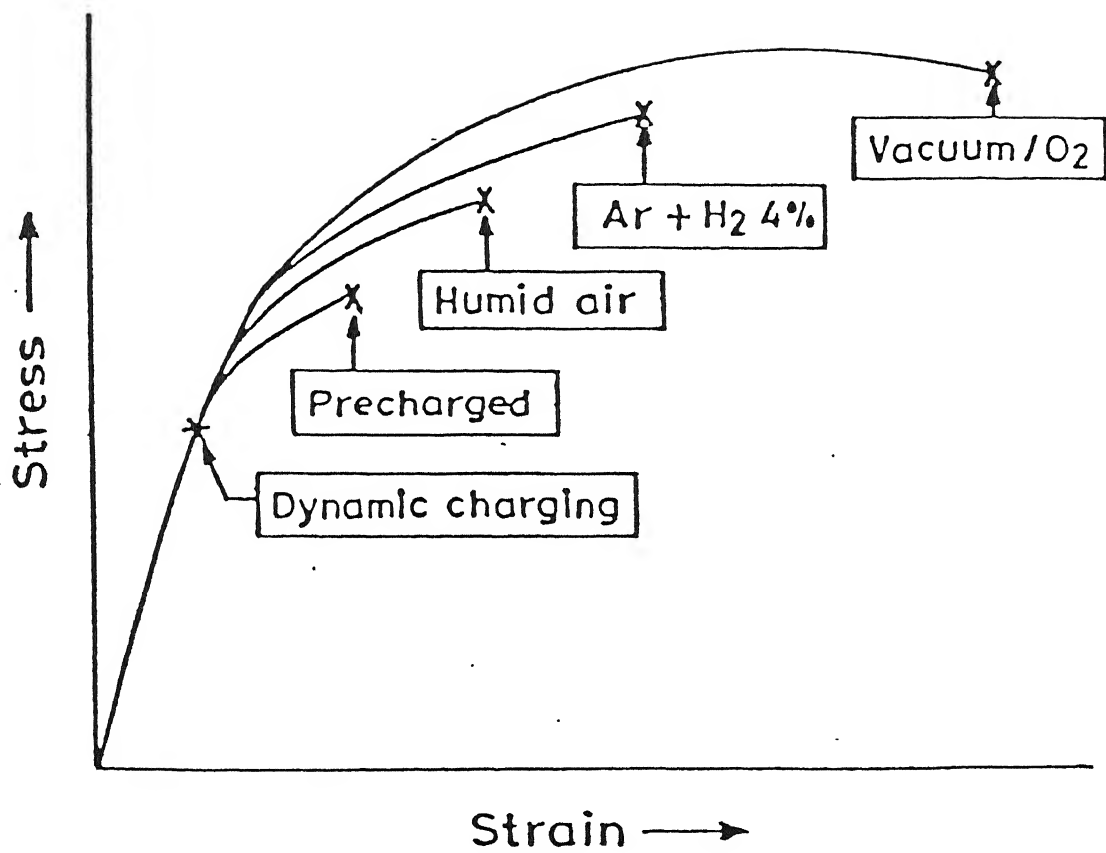
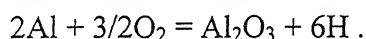


Figure 3 Schematic tensile stress-strain behavior of iron aluminides in various environments at ambient temperature

In order to obtain the desired properties of metals, alloying with additional elements is generally attempted. The type alloying addition would depend upon the property that is being addressed. For providing strength, elements that lead to solid solution strengthening or to the precipitation of age hardenable phases are added. This could also be increased by adding elements that refine the grain size and hence provide grain strengthening. In case the corrosion resistance of the metal has to be enhanced, passivity-inducing elements should be added. It should be emphasized that the alloying element that is added should not lead to the deterioration in some property where it is not intended. For example, if an element primarily added to enhance passivity, leads to the precipitation of ternary brittle intermetallics, especially at the grain boundaries, the property of strength would be very severely affected. therefore, the possible deleterious effects of alloying should also be understood.

2.3 Hydrogen Embrittlement Mechanism

The process of HE in iron aluminides can be visualized as follows. The reaction that provides nascent hydrogen which embrittles iron aluminides is



The propensity of this reaction increases with increasing aluminium concentration in iron aluminides [11]. The reaction of condensed moisture from ambient environments with aluminium at crack tips and freshly created metal surfaces (due to oxide spallation) results in the generation of high fugacity atomic hydrogen that causes embrittlement. This process is schematically illustrated in Figure 4.

Birnbaum *et al* have proposed a mechanism known as hydrogen enhanced localized plasticity (HELP) [14]. This mechanism suggests that hydrogen increases plasticity at the crack tip in many metals and alloys, leading to brittle fracture. There is a controversy about this mechanism that whether hydrogen influences plasticity through the volume of surface. But there are enough evidences to prove slip localization due to hydrogen near a crack tip in several fcc and bcc metals [14]. However, in the case of iron aluminides, the fracture is essentially of cleavage type in the presence of hydrogen and therefore HELP mechanism may not be applicable to the case of iron aluminides.

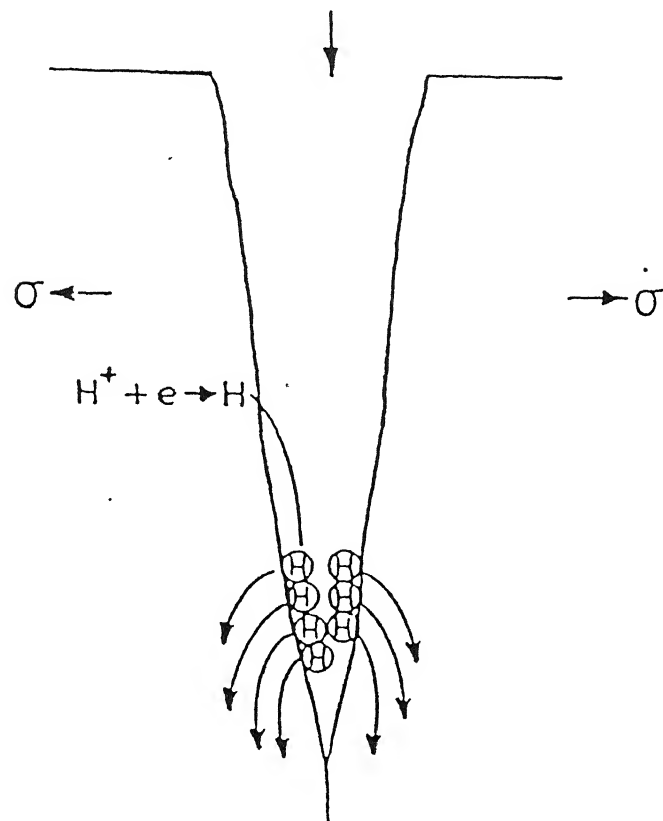
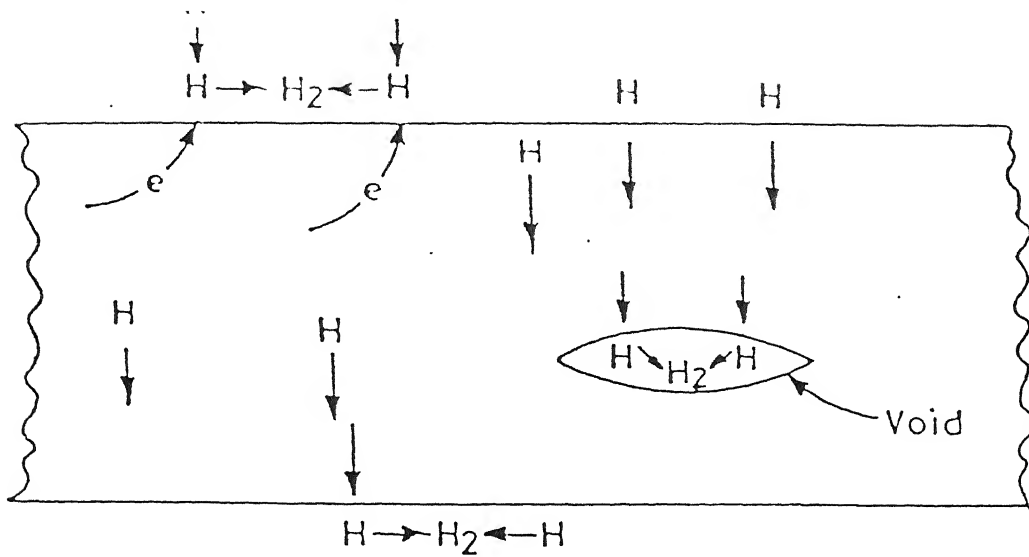


Figure 4 Hydrogen entry into the material and processes, that occur at the crack tip during hydrogen embrittlement

Generally, the appearance in this class of intermetallics is of the cleavage type, with facets of $\{100\}$ type suggesting “ decohesion “ as the possible mechanism of hydrogen embrittlement. The decohesion mechanism of hydrogen embrittlement is shown in Figure 5. Hydrogen enters the material after bulk diffusion or grain boundaries diffusion and adsorption on the surface. This hydrogen is supposed to lower the bond strength in iron aluminides [8]. Evidence for decohesion mechanism is based upon the brittle appearance of fracture surface and the propensity for cleavage on $\{001\}$ planes in embrittled single crystals of intermetallic aluminides [16]. Moreover, the brittle appearance of hydrogen induced (or moisture induced) fatigue cracks in iron aluminides alloys also suggests ‘decohesion’ as the likely mechanism of hydrogen embrittlement [16]. In an entirely study, the presence of etch pits indicated the emerging points of some of these dislocations [17]. Most of these etch pits were of rectangular shape which indicated that the cleavage were of the $\{100\}$ type. Therefore, the cleavage planes in Fe_3Al being of the $\{100\}$ is not surprising as the structure of Fe_3Al is essentially BCC (i.e. disordered α at high temperature and ordered B2 and DO_3 at lower temperatures). The appearance of $\{100\}$ cleavage facets suggests decohesion as the possible mechanism for hydrogen embrittlement (HE) in this class of intermetallics. Hydrogen enters the material and is transported to potential flaw sites by bulk or grain boundary diffusion or by dislocations sweeping in of hydrogen. The incoming dislocations are locked as immobile $\langle 100 \rangle$ dislocations [8]. Locked dislocation networks of this type have been observed by transmission electron microscopy with in the grains and grain boundaries [18] of deformed iron aluminides. Hydrogen promotes the formation of these locked $\langle 100 \rangle$ dislocations [19] and twice the amount of normal hydrogen can be trapped by these dislocations [19]. The amount of hydrogen should exceed a critical level to cause cracking, as is well known in hydrogen embrittlement phenomenon. The critical limit to cause cracking should be a function of the stresses created in the hydrogen occupied interstitial sites on the $\{100\}$ planes of the ordered B2 and DO_3 structures. The actual number of tetrahedral sites would depend upon the type of crystal structure (B2 and DO_3) but their presence in sufficient quantity aids hydrogen accumulation on the $\{100\}$ plane leading to cracking by decohesion [8].

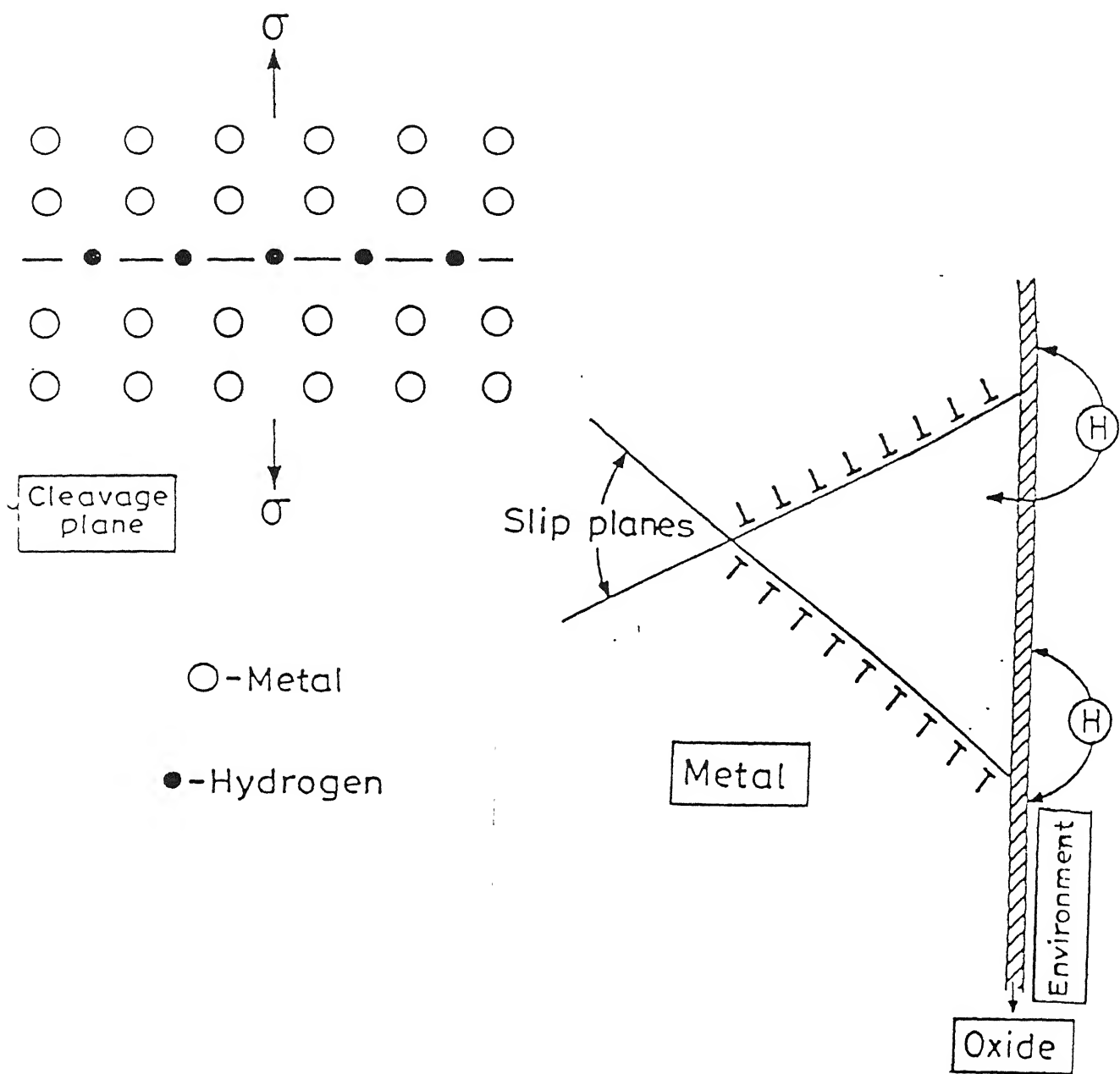


Figure 5 Hydrogen embrittlement mechanism by the decohesion mechanism in iron aluminides

2.4 Hydrogen Diffusion in Iron Aluminide

The pronounced susceptibility of iron aluminides to hydrogen embrittlement may be a consequence of ordering effects on diffusion behavior or of an enhanced fracture mechanism. Long range order generally is considered to slow diffusion. However, extensive experimental data on room temperature diffusivity of hydrogen in iron aluminides is lacking. It has been already reviewed that cracking caused in iron aluminides is due to hydrogen. Recently Zhu *et al* have provided a direct evidence of hydrogen generation from the reaction of water with Fe-38.5Al using laser desorption mass spectroscopy [12]. The following subsections review the entry of hydrogen and its effect on the substructure of iron aluminides.

The diffusivity of hydrogen in four iron aluminides was determined by the technique of subscale microhardness profiling. The diffusivity of hydrogen (in m^2/s) is $1.46 \cdot 10^{-14}$ in Fe-28Al, $4.37 \cdot 10^{-15}$ in Fe-28Al-2Cr, $5.45 \cdot 10^{-15}$ in Fe-28Al-2Ti and $4.98 \cdot 10^{-15}$ in Fe-28Al-1Cr-1Ti [28]. Similar values were obtained after hydrogen charging in NaCl solution. The important conclusion was that alloying with Cr or Ti lowers the diffusivity of hydrogen by an order of magnitude compared to the base intermetallic [28]. The diffusivity of hydrogen in Fe-38Al was also estimated by mathematical analysis of hydrogen concentration versus depth data obtained by Zhu *et al* [12] by applying the standard equation. It was found to be $2.38 \cdot 10^{-15} \text{ m}^2/\text{s}$ at room temperature. This is the first reported value of hydrogen diffusivity in Fe-35.8Al [20]. This value of hydrogen diffusivity is a lower bound value.

As regards diffusivity of hydrogen in pure Al and α -Fe, there are several published reports that are available. The topic of hydrogen diffusion in pure α -Fe has been reviewed by Völkl and Alefeld [21,22] and by Kiuchi and McLellan [23]. Figure 6 [21] and Figure 7 [23] show the values of diffusion coefficient of H in α -Fe obtained by various researchers. The feature that is to be observed is the relative large scatter in the experimental diffusivity data for hydrogen in iron, especially for temperatures lower than about 300K. This has been attributed to the errors in the experimental procedure which

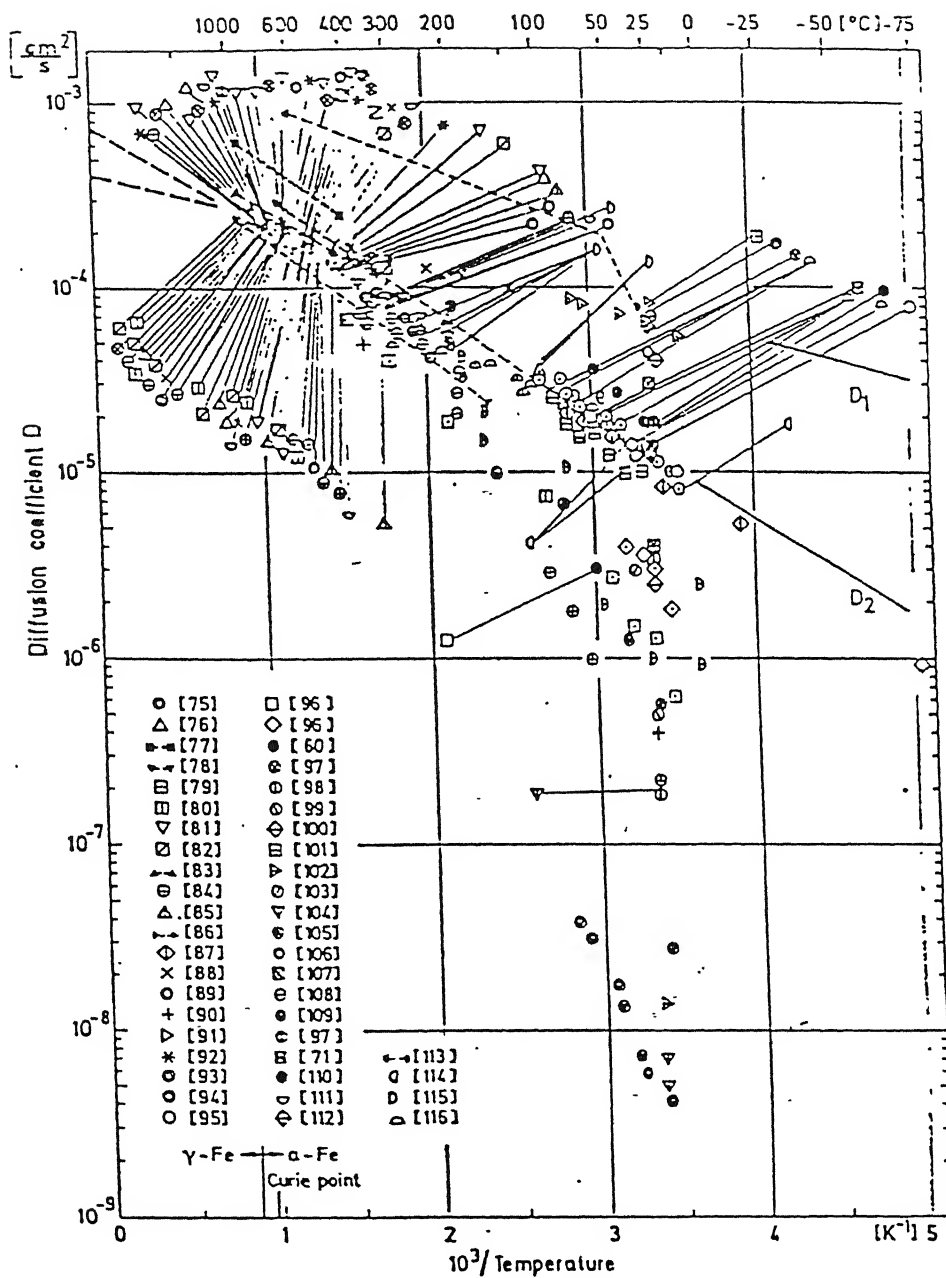


Figure 6 Diffusivity of hydrogen in α_{Fe} . Number in brackets refer to literature cited in reference 8

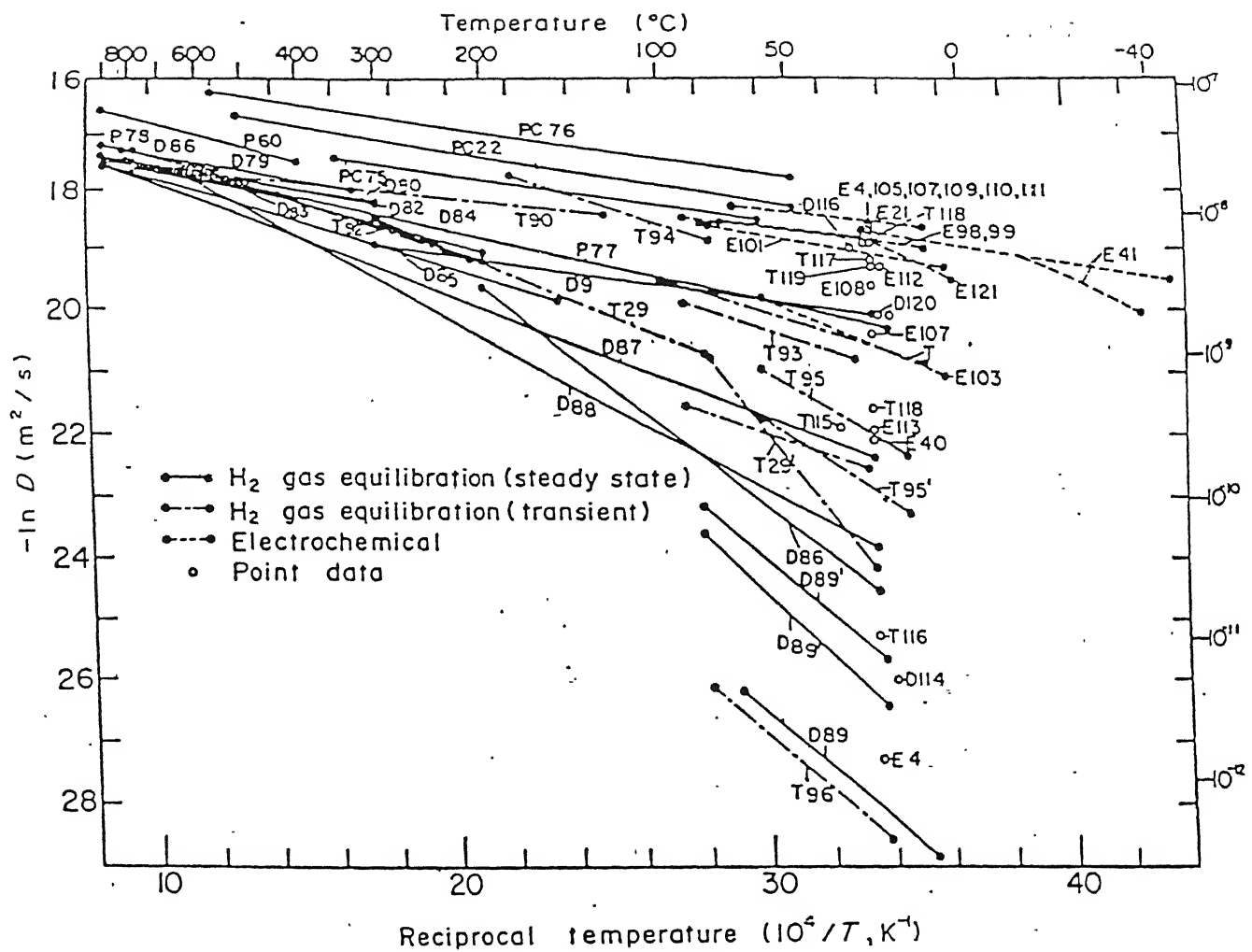


Figure 7 Arrhenius representation of diffusivity of hydrogen in $\alpha\text{-Fe}$ [23]

normally result in lower hydrogen diffusivity due to surface effects, defects in the surface regions like trapping sites, defects in the bulk regions like dislocations and impurity atoms, and surface oxide effects [23]. From these figures, it can be seen that the room temperature diffusivity of hydrogen varies from $10^{-8} \text{ m}^2/\text{s}$ to $10^{-12} \text{ m}^2/\text{s}$.

Chiu *et al* have employed an electrochemical permeation technique to measure the room temperature diffusivity of an alloyed Fe_3Al -based alloy, recently [24]. They were ordered to get a B2 structure. The calculated diffusivity value was of the order of $10^{-9} \text{ m}^2/\text{s}$ which they claimed was reasonable based on the fact that hydrogen diffusivity in bcc metals at room temperatures were of the same order magnitude.

2.5 Minimizing Hydrogen Embrittlement

The main drawback of using iron aluminide as structural material is the low room temperature ductility and this is assigned due to the hydrogen embrittlement at room temperature. The embrittlement involves the reaction of the moisture in air with Al in Fe_3Al and FeAl and generation of atomic hydrogen, resulting in moisture induced hydrogen embrittlement in moist air. The reaction of moisture with iron aluminides has been evidenced directly by observing the formation of Al oxide films on specimen surfaces and the detection in iron aluminides of hydrogen released from water vapour [12,25].

Because of this finding, considerable research effort has been expended to find metallurgical ways to reduce moisture induced embrittlement and to increase the tensile ductility of iron aluminides at room temperature. It has been reported that environmental embrittlement can be alleviated by alloying additions, control of surface conditions, change in crystal structures and control in grain shape.

2.5.1 Ductility Improvement by Alloying

Alloying addition has been one of the schemes used to improve the ductility of iron aluminides. Alloying control, surface condition, reduction in hydrogen solubility and diffusion, refinement of grain structure, enhancement of grain boundary cohesion, grain shape and recrystallization condition [3].

Of the several methods which have been adopted to minimize HE of iron aluminides, chromium additions have been very useful in increasing ductility by an order of magnitude [27]. Table 3 summarizes the tensile behavior of iron aluminides where the effect of chromium addition can be observed [27].

McKamey and Liu have earlier suggested that the beneficial effect of Cr comes from surface oxide modification, rather than modification of bulk properties [5]. They suggested a change in oxide chemistry and properties or a change in kinetics of oxide formation, thereby reducing the water-vapour reaction. The mechanism for the increase in ductility by Cr additions has been elucidated by the mixed potential theory by Balasubramaniam [8] wherein proposed that alloying with Cr includes passivity which results in reduction in the rate of hydrogen liberation and therefore reduces the amount of hydrogen enters the lattice to cause embrittlement. This mechanism suggests that the entry of hydrogen into the lattice can be checked and HE minimized by alloying passivity-inducing elements to iron aluminides.

Boron addition (in ppm range) has been found to be very effective in increasing the grain boundary cohesiveness in ordered intermetallic alloys [29]. Boron has also been effective for Fe-Al class of aluminides. Boron segregates at grain boundaries and reduces intrinsic brittleness of B2 iron aluminide [30].

Zirconium, has been alloyed to Fe₃Al to strengthen grain boundaries and to prevent recrystallization [31]. McKamey and Pierce have already confirmed that, partially recrystallized microstructure reduces hydrogen embrittlement [31]. Therefore zirconium additions can help in minimizing hydrogen embrittlement.

Liu et al have studied the effect of Ti addition to Fe₃Al on the mechanical behavior of at high temperatures [32]. They have demonstrated superplastic behavior in the Fe₃Al-2Ti alloy at high temperature. Interesting, this alloy showed superplastic behavior even at large grain size of 100µm. This has been ascribed to the process of dynamic recovery and recrystallization occurring in Fe₃Al-2Ti intermetallic at high temperatures.

Yangshan *et al* [33] have shown that cerium addition to a very small extent increases the ductility of base Fe-28Al and Cr-alloyed iron aluminides significantly. They proposed that Ce additions accelerated the formation of aluminium and chromium oxides which passivated the specimen surface thus preventing hydrogen from diffusing into the

Table 3 : Room temperature mechanical properties of Fe-28Al and Fe₃Al + Cr alloys [27]

Alloys	Yield strength(MPa)	UTS (MPa)	Ductility(%)
Fe-28Al	279.2	514.4	3.7
Fe-28Al-2Cr	247.2	638.5	9.4
Fe-28Al-4Cr	228.2	553.4	8.2
Fe-28Al-6Cr	232.4	535.4	8.4

specimen. They have also shown that Ce additions caused partially ductile failure instead of brittle failure in the iron aluminides without Ce addition. Addition of Ce also produced a fine grain structure after complete recrystallization in contrast to the large grain size observed without Ce additions. Therefore, the strength properties were not significantly reduced upon complete recrystallization in the Ce-alloyed iron aluminides. They also observed precipitates rich in Fe, Al and Ce to form in the grain boundary regions of the Ce alloyed intermetallics. It is reasonable to assume that the Ce containing phase acts as

irreversible traps for hydrogen and therefore, lowers the amount of hydrogen present in the material, thereby delaying embrittlement. Interestingly, the addition of Ce had also changed the composition of the surface passive film. With the addition of Ce, the surface layer contained a larger amount of Al_2O_3 and Cr_2O_3 and a lower amount of Fe_2O_3 than the Fe-28Al-2Cr alloy without Ce addition. Therefore, the presence of strong hydrogen trapping compounds, homogeneously distributed throughout the iron aluminide matrix, could also be beneficial in delaying embrittlement.

In view of this, a small amount of Mm (Indian Mischmetal, a mixture of rare earth elements) was added to the Cr and Ti alloyed iron aluminides [26,28]. The Mm added had the composition, in weight percent, 43 Ce, 23 La, 18 Nd, 5 Pr, 3 Sm and 8 Fe. The main aim of adding Mm was to observe if enhanced room temperature ductilities would obtain. However, the Mm-added intermetallics were fairly brittle. Microstructural analysis indicated that several grain boundaries had cracked during processing. The EPMA analysis of the composition at grain boundaries that had cracked after the thermomechanical processing operation indicated that the major elements that constitute Mm (namely Ce, La and Nd) were enriched at the grain boundaries. La was analyzed to be present only at grain boundaries. The poor ductilities obtained in the alloyed aluminides has been attributed to the presence of these elements (either in their elemental form or in the form of precipitates) along the grain boundaries which resulted in grain boundary weakening and to initiation of surface cracks during the rolling operation. Therefore, careful control of Mm (or Ce) addition may be required to render the iron aluminides ductile [26].

2.5.2 Ductility Improvement by Thermomechanical Processing

Strength and ductility of iron aluminides are strongly affected by processing schedule and cooling rate. Workers have shown that ingot metallurgy route followed by thermomechanical treatments significantly increase the tensile properties.

It is important to mention that recrystallization processes vary greatly in the iron aluminide system with several variables such as thermo-mechanical treatments, alloying, crystal structure and microstructure [34]. Thus it is difficult to predict exactly about recrystallization temperature and kinetics in the iron aluminide system.

McKamey and Pierce have studied the effect of annealing temperature on the mechanical behavior of iron aluminide [31]. From their study it is clear that ductility improves after annealing treatment at 750°C for 1 hour. This treatment produces a stress relieved but partially recrystallized microstructure. A completely recrystallized microstructure produces least desirable mechanical properties. These results indicate that a stress relieved and partially recrystallized microstructure minimizes environmental embrittlement in iron aluminides. The exact mechanism of minimizing embrittlement by controlling microstructure is yet unresolved. One of the mechanism suggests that elongated grain structure characteristic of as-rolled and partially recrystallized structures provide a minimum of transverse cleavage planes as well as a minimum of grain boundary area. This suppresses the atomic hydrogen ingress and also the grain boundary diffusion of hydrogen is reduced. Hence, the extent of hydrogen embrittlement is also minimized [31]. However, it is difficult to imagine that the diffusivity of hydrogen would be very much different in the grain boundary and bulk regions of iron aluminides and therefore the reason for ductility enhancement in the case of the partially recrystallized microstructure could be due to some factor. 13

It has been hypothesized that this is due to the unrecrystallized grains disrupting the diffusion of hydrogen [31]. This may not be the reason as hydrogen can diffuse with relative ease in the iron aluminide matrix and grain boundaries. A possible reason for enhancement of ductility due to the unrecrystallized structure could be the reduction in the dislocation density during stress annealing treatment [35]. The gliding $a\langle 111 \rangle$ dislocations in Fe_3Al are composed of two $a/2\langle 111 \rangle$ partials joined by an anti phase boundary [34]. Hydrogen is transported primarily by these partial dislocations deep down into the material. Further, the partial dislocations can be locked as immobile $a\langle 100 \rangle$ dislocations by the Friedel mechanism. It has been shown that hydrogen promotes the formation of locked $\langle 100 \rangle$ dislocation and twice the normal amount of hydrogen can be absorbed by these locked dislocations [36]. According to all theories of hydrogen embrittlement, the concentration of hydrogen should exceed a critical amount to cause embrittlement and this critical concentration is achieved in the $\{100\}$ planes due to the above reason [8]. Once the critical concentration is achieved, hydrogen causes decohesion of the matrix and this is verified by cleavage fracture observed in this class of iron aluminides [37]. Moreover, etch pit studies

have indicated that the cleavage facets are of the $\{100\}$ type [17], further confirming the above mechanism. The improvement in ductility upon stress relieving the microstructure could therefore be due to the reduction in the number of $a/2\langle 111 \rangle$ dislocations in the structure during annealing treatment. With a lower amount of $a/2\langle 111 \rangle$ partials in the microstructure, the local accumulation of hydrogen and the locking of partials would be less severe and hence this would result in enhanced ductilities, as observed experimentally [17,31].

There is a sacrifice in strength upon the recrystallization treatment. Complete recrystallization would lead to a large decrease in strength [31] and therefore, not a viable alternative. The exception to the above would be when the alloying addition produces a fine grain size after the recrystallization anneal in which case the strength would not decrease drastically. Interestingly, Ce additions to iron aluminide produces a fine grained recrystallization structure unlike the large grain size obtained for the iron aluminide without Ce addition and there is no degradation of strength for the Ce alloyed iron aluminide even in the recrystallized condition [33]. Therefore, the addition of elements to inhibit recrystallization would also be beneficial in improving the room temperature ductility of iron aluminides.

2.5.3 Surface Modification

The effect of surface modifications on the hydrogen embrittlement behavior of iron aluminides can be seen Table 4 [28]. The surface nature can be manipulated by several methods such as electropolishing, oxide coating, metallic coating and alloying. The first two aspects were studied in detail by McKamey and Liu [28]. Tensile tests were carried out on iron aluminides having the following surface conditions (a) electropolished surface, (b) as received (as rolled) condition consisting of a thin film formed during rolling, and (c) oxide coated (by oxidizing iron aluminide in air). Table 4 summarizes the tensile behavior of these specimens.

It is obvious from Table 4 that ductility increases upon oxide coating. Several other inferences can also be drawn from Table 4 concerning Cr coating iron aluminides. In the samples which were electropolished and then annealed in vacuum to minimize oxide reformation, ductility comparable to the binary Fe-28Al intermetallic in both the B2 and DO_3 ordered conditions were obtained. There was a significant increase in ductility for Cr containing samples as compared to the base Fe-28Al intermetallic in the as rolled condition. Chromium containing specimens which were heat treated for 96 hours at 500°C in air (to give the DO_3 crystal structure) showed comparable ductilities, whether

Table 4 : Effect of surface condition on room temperature properties of Fe-28Al [5]

Crystal structure	Surface condition	Yield strength(MPa)	UTS(MPa)	Elongation(%)
B2	Electropolished	387	559	4.1
	as rolled	398	587	4.3
DO3	Electropolished	267	515	5.4
	as rolled	277	551	5.6
DO3	Oxide coated as	270	429	3.6
	rolled	285	466	3.6

they were oxide coated or present in the as rolled condition. Also, the ductility of the oxide coated (Cr containing) intermetallic was higher than the electropolished specimen. These results strongly suggested that surface passive films on iron aluminides restrict hydrogen embrittlement.

It has also been shown that metallic coatings of Cu and Ni on iron aluminide of composition Fe-28Al -5Cr -0.5Mo-0.5Nb-0.05B-0.05Zr were effective in minimizing the environmental embrittlement [6]. The coatings were applied by electro-brush plating. Plating with Cu was shown to be more effective in inhibiting embrittlement. The fracture morphology changed from transgranular cleavage for non-coated specimens to a mixed one of dimple fracture and transgranular cleavage for the coated specimens. An inner layer was found between the copper coating and the matrix which was formed by reaction of the copper with the iron aluminide matrix.

2.5.4 Ductility Improvement by Passivity Induction

As seen earlier, the most effective alloying addition that results in ductility enhancements is Cr. Even Cr additions as low as 2% has been reported to be effective in providing improved ductilities [27] . The role of Cr in minimizing embrittlement has been elucidated electrochemically by the mixed potential theory [8], according to which the induction of passivity by the addition of Cr reduces hydrogen liberation rates on the surfaces of Cr-alloyed iron aluminides when compared to the base intermetallic.

The potentiodynamic polarization curves of base Fe₃Al and Cr-alloyed Fe₃Al have been theoretically deciphered and it was how that on alloying with Cr, the mixed potential of the intermetallic is established in the passive region at a potential noble to the reversible hydrogen potential [39]. Table 5 summarizes the following findings. Moreover, the passive layer would also hinder hydrogen entry into the lattice. In view of the beneficial effect of surface passive films in lowering the HE of iron aluminides [40], an alloy development philosophy was proposed where in it was stated that elements that induce passivity in iron when added to Fe₃Al would inhibit hydrogen reduction and its entry by maintaining a passive layer [8,35].

Several passivity inducing elements (Ti, Zr, V, Nb, Ta, Cr, Mo, W, Si and Ni) have been alloyed to the base Fe₃Al intermetallic (to produce Fe₃Al-5M intermetallics) in order to test the ductility enhancement philosophy [41] . Ni could not be alloyed due to a violent reaction with the

passivity concept

Table 5 : Effect of surface metallic coatings on the room temperature mechanical properties of iron aluminide [38]

Surface condition *	Film thickness	U.T.S.(MPa)	Y.S. (MPa)	Elongation (%)
POL	----	798	644	6.1
AOQ	----	650	960	12.0
EBP(Cu)	1 μ m	1154	754	15.6
	3 μ m	1148	720	16.5
	6 μ m	1162	752	18.2
EBP(Ni)	1 μ m	996	743	9.4
	6 μ m	1156	754	16.6

POL = polished, EBP = electro-brush plating

AOQ = annealed 1 hr/700°C + oil quenched

intermetallic on mixing, which is possibly due to the large exothermic heat of mixing between Ni and Al [42]. Electrochemical polarization studies of the alloyed intermetallics in acidic 0.05 mol/l H_2SO_4 solution indicated that all the intermetallics, bearing the V-alloyed one, induced passivity to the base iron aluminide exhibited active corrosion in this medium. Therefore, passivity enhancement upon addition of these elements has been verified. The base Fe_3Al [17] and the alloyed intermetallics [41] were thermomechanically processed at 1000°C by multi-pass rolling after a homogenization treatment (in order to make the composition of the buttons uniform). It was observed that only the Fe_3Al , $\text{Fe}_3\text{Al-5Cr}$ and $\text{Fe}_3\text{Al-5Ti}$ intermetallics could be rolled successfully to 80% deformation in multiple passes at 1000°C . The Cr and Ti alloyed intermetallics also exhibited significant ductilities at room temperature [41]. The $\text{Fe}_3\text{Al-5Ta}$ intermetallic cracked after 50% deformation and the $\text{Fe}_3\text{Al-5Nb}$ intermetallic cracked after 40% deformation. The $\text{Fe}_3\text{Al-5Mo}$, $\text{Fe}_3\text{Al-5Si}$ and $\text{Fe}_3\text{Al-5V}$ could not be rolled as they cracked in the first rolling pass itself. Thermomechanical processing of the intermetallic is also an important aspect of alloy development as the material should be amenable to deformation processing from a commercial angle. Although the alloy additions induce passivity in the base intermetallic, the poor thermomechanical response of the intermetallics alloyed with Ta, Nb, Mo, Si and V was poor due to the formation of brittle phases. A detailed fractographic and microstructural study of the other alloyed intermetallics revealed the precipitation of brittle phases on alloying Ta, Mo, V, Nb, and Si to Fe_3Al [37]. These intermetallics could, therefore, be important that the addition of passivity-inducing elements should not lead to brittle intermetallic precipitation. If this is taken care of then the hydrogen embrittlement (HE) could be minimized and higher room temperature ductilities can be achieved with these alloying additions. Moreover, the element(s) would provide additional solid solution strength to the base intermetallic.

2.5.5 Irreversible Hydrogen Trapping

One of the impediments to the commercial application of iron aluminides is their poor room temperature ductility, which is due to their susceptibility to hydrogen embrittlement (HE). It is well known that hydrogen has to be accumulated at certain region in the lattice and once a critical hydrogen concentration is achieved, HE occurs. In this regard, both reversible and irreversible trapping of hydrogen has to be considered. Trapping of the hydrogen in the metal is likely to affect the HE. It is well known that certain elements or compounds when present in alloys act as trap sites for hydrogen. Traps can be classified as either reversible or irreversible, based on the binding energy

of traps with hydrogen. They may be mobile (dislocations) or stationary (solute atoms, particles, grain boundaries) [49]. For, example Ti in steel acts like a reversible trap while incoherent TiC precipitates in steels are irreversible traps (due to trapping at the inclusion-matrix interface) [50].

Because traps are associated with various microstructural features, alloying and metallurgical treatments to modify trapping properties offer a promising avenue to the development of alloys with maximum resistance to hydrogen damage. Deep or irreversible trapping reduces the population of hydrogen at the crack tip and often increases resistance to hydrogen induced cracking (HIC) [49]. Conversely, shallow or more reversible traps permit more rapid hydrogen transport, which allows some traps to reach a critical concentration necessary to initiate cracking.

If the irreversible traps are finely and homogeneously distributed throughout the matrix, there is a good likelihood that hydrogen would be irreversibly trapped at these sites and hydrogen can not accumulate at critical regions to cause embrittlement. Therefore, addition of elements or compounds which can act as irreversible traps for hydrogen could also be envisaged to improve ductility of iron aluminides. However this may not be promising route because there would be sufficient accumulation of hydrogen, with time, at these locations and once the hydrogen concentration exceeds the critical concentration for embrittlement, the material would be susceptible to embrittlement [50]. It should be noted that hydrogen appears to be generally trapped reversibly in both Fe-25Al and Fe-35Al based on the reversible nature of embrittlement (i.e. recovery of ductility on baking treatments).

Recently Baligidad *et al* have reported that addition of carbon in the range of 0.14 to 0.50 wt% significantly increases the room temperature strength of Fe-16 wt% (28 at%) Al alloys [9]. These alloys also exhibited good room temperature ductility. The improvement in ductility on C addition to iron aluminide also must be related to irreversible hydrogen trapping at the Fe_3AlC precipitates [13]. This Fe_3AlC phase has FCC crystal structure with Al atoms at the corner positions, Fe atoms at the face centered positions and carbon atom at the body centre position (i.e. at the octahedral void) in the cube.

Chapter 3

Experimental Procedure

The aim of this work is to understand the effect of carbon additions in iron aluminide on several mechanical and environmental degradation properties. This involved microstructural characterization, mechanical behavior characterization and electrochemical characterization. Moreover, hydrogen diffusivity and effect of hydrogen charging behavior on microstructure were also studied. All the experiments were designed and carried out with the above aims in mind.

3.1 Materials

The carbon alloyed iron aluminides were obtained from DMRL, Hyderabad. Their composition (in at%) were Fe-28.1Al-2.1C (ESR56) and Fe-27.46Al-3.66C (ESR63). In terms of wt%, the compositions were Fe-16.2%Al-0.54%C (ESR56) and Fe-16.0%Al-0.9%C (ESR63). Here, ESR stands for electro-slag remelted specimens. These materials were obtained from DMRL, Hyderabad, in the form of metal strips of dimensions 120 mm × 57mm × 3.01mm and 110mm × 95mm × 2.97mm for ESR56 and ESR63, respectively. The processing technique utilized to obtain these strips was as follows [43].

The iron aluminide ingots containing 15.55wt% Al (28 at%) were prepared by air induction melting (AIM) and chill casting into cast iron moulds. Commercially purity aluminium and mild steel scrap were used as raw materials. The surface of the iron charge was cleaned by grinding. After melting, the slag product was skimmed off. Aluminium pieces were then added to the molten iron bath. The melt was held at 1620° C for a very short time (2 minutes) to prevent aluminium losses. The ingots were tested for

their soundness in a radiography unit. These AIM ingots (55 mm dia., 360 mm long) were machined to 50 mm diameter for refining in an ESR furnace of 350 kVA capacity. A commercial prefused flux based on CaF_2 was used. The flux was preheated and held at 850°C for 2 hours before use to remove moisture. The iron aluminide electrode was remelted under flux cover and cast into 76 mm ingot in a water cooled steel mould. At the end of the process, the power supply was gradually reduced to impose a condition of hot topping. To check their soundness, the ESR ingots were also radiographed. The ingots were now forged to a reduction ratio of 70% and after forging they exhibited recrystallized grains [43].

3.2 Polarization Studies

Square sections of 1 cm side for each specimens ESR56 and ESR63 were mounted in a cold setting epoxy with conductive wire. Specimens surfaces were polished to 600 grit surface finish and were properly cleaned with acetone prior to polarization experiments. Polarization experiments were performed in an electrochemical polarization cell controlled by a potentiostat (EG&G 273 model with a built-in microprocessor) interfaced to personal computer. A platinum foil of 1 cm^2 area was used as the counter electrode. A 0.05 mol./l H_2SO_4 solution ($\text{pH} = 1$) and buffer solution (0.15N H_3BO_3 + 0.15N $\text{Na}_2\text{B}_4\text{O}_7 \cdot 10\text{H}_2\text{O}$, $\text{pH} = 8.44$) are the electrolytes used in the present study. Before the polarization experiment, the specimens were immersed in the electrolyte and the free corrosion potential (FCP) was monitored as a function ^{of} if time. The FCP stabilized usually in a short time. Once the steady state FCP were obtained, the polarization experiment was performed at the rate of 1 mV/sec. The potential was scanned from the active to noble direction. The temperature of the polarization cell was not controlled and all experiments were performed at ambient temperature (25°C). The potential was monitored continuously versus standard calomel electrode (SCE) attached to the luggin capillary. All potentials referred in this thesis are with respect to SCE. The corrosion rates were determined from the polarization diagram, using both the Tafel extrapolation and linear extrapolation technique. [48].

3.3 Hydrogen Diffusivity

Hydrogen diffusivity was estimated from subscale microhardness profiles obtained after hydrogen charging. Samples, approximately 10mm X 10mm X 3mm in dimensions were sectioned from the given samples. All the surfaces were ground up to 600 grit level and cleaned with acetone prior to hydrogen charging. Cathodic charging of hydrogen was performed in electrochemical cell, where specimens were used as cathode and platinum foil used as anode. A 0.05 mol/l H_2SO_4 solution, to which 100ppm of arsenate ion was added as a hydrogen 'poison', used as the electrolyte. Hydrogen was charged at a constant cathodic current density of 10 mA/cm^2 for 12 hours. At the end of the experiments, the samples were immediately mounted in cold setting epoxy. The cross sections were initially ground up to 600 grit level and later metallographically polished to $1 \mu\text{m}$ finish. Microhardness measurements at interval of $20 \mu\text{m}$, were taken along the cross section of the polished specimens. Six microhardness profiles were measured for each specimen.

3.4 Microhardness

Microhardness measurements of specimens were performed using a Leitz Wetzlar Miniload microhardness Tester attached with a microscope. A diamond pyramid indenter with a 50 grams load was employed. Observations were made at a magnification of 500X. Several microhardness values were measured for each specimens. All the values are noted as Vicker's hardness number (VHN) which was obtained from

$$\text{VHN} = 1854.4 * P/d^2$$

where P is the load in gms and d is the diameter of indentation mark in μm .

3.5 X-ray Diffraction

X-ray diffraction (XRD) patterns of the carbon alloyed iron aluminides were recorded with a Rich-Siefert 2002 X-ray diffractometer using CuK_α radiation. The scan rate was fixed at $3^\circ/\text{min}$. and the chart speed was fixed at 3 cm/sec and scanned between

10° to 138°, as in previous work Fe-28Al-2Cr sample (without carbon) was scanned between 20° to 120°. A magnification of 5K was used in all recordings.

3.6 Immersion Testing

The electrochemical methods of determining corrosion rates (i.e. Tafel extrapolation methods) were complemented with long term mass-loss immersion tests. This provides information about the time dependence of the process involved. Specimens of known surface area were polished to 600 grit, degreased with acetone, weighed and were immersed in 0.05 mol/l H₂SO₄ solution. The specimens were removed from the solution and the corrosion products were just washed off using distilled water. Then the specimens were weighed after specific intervals of time. The specimens were again immersed in the solution after the reading was obtained. Both the alloys were immersed for a total of 24 hours span of time and were weighed after every 30 minutes interval in the first set of experiment. In second set of experiment to study the long term corrosion effect, the samples were immersed for total of 8 days and were weighed after every 12 hours. In all the cases, the corrosion rate (C.R.) is given by

$$\text{C.R. (in mmpy)} = (k \times W) / A \rho t$$

where W is the weight loss (precision of 0.0001gm), A is the surface area of the specimen to the nearest 0.01 sq. cm, t is the time of exposure in hours, ρ is the density in gm/cc. k is a constant and its value is 87×10^3 for obtaining corrosion rate in mm per year (mmpy) [44]. However the temperature was not controlled during the experiments and the experiments were conducted at different climatic conditions. Therefore, temperature varied between 20°C and 35°C.

3.7 Mechanical Testing

Several tensile specimens are prepared from the rolled ESR56 and ESR63 strips with the gauge length parallel to the rolling direction as well as the transverse direction. Duplicate tensile testing of both ESR56 and ESR63 was maintained. The flat samples were machined to obtain tensile test specimens of 25 mm gauge length, 9 mm width and 3.01 mm thickness. One set of tests was performed on the uncharged hydrogen specimens

for both ESR56 and ESR63. Before performing the tensile test each sample was baked at 250° C for 1 hour. Baking was performed to remove the reversibly trapped hydrogen from the material. To minimize hydrogen entry into the lattice of intermetallic during the testing, each sample was coated with silicone oil before testing. Tensile testing was done on an Instron testing machine at a constant strain rate of 10^{-4} sec^{-1} .

The second set of tensile specimens was prepared the following way. The tensile test sample was used as a cathode in an electrolytic cell. The electrolyte used was 0.05 mol/l H_2SO_4 solution. Platinum electrode was used as the anode and sodium arsenate was used as hydrogen 'poison' in this experiment. Hydrogen was charged for 12 hour at a current density of 10 mA/cm^2 . After hydrogen charging the sample was baked at 250°C for 1 hour. This procedure ensures that all the reversibly trapped hydrogen is removed as hydrogen is bound less tightly with reversible trap sites [47], and only irreversibly trapped hydrogen remains in the sample. Then, the sample was coated with silicone oil to restrict the hydrogen diffusion during tensile testing, to and from the sample. The sample was tensile tested on the same machine with same specification.

3.8 Optical Microscopy

The microstructures of both the samples (ESR56 and ESR63) were observed, in both the rolling as well as transverse directions, by an optical microscope (Leitz Laborlux 12 MES microscope). Each sample was polished up to 600 grit level and then fine polished by $0.5 \mu\text{m}$ Al_2O_3 powder. For revealing the microstructure, the following etchant was used : 33% acetic acid (CH_3COOH), 33% nitric acid (HNO_3), 33% water and 1% hydrofluoric acid. Optimum etching time was fixed for 12 seconds.

3.9 Scanning Electron Microscopy

Scanning electron micrographs were obtained for both the samples ESR56 and ESR63 at higher magnification in scanning electron microscope (SEM) (JEOL JSM 840A). The samples were finely polished upto $0.5 \mu\text{m}$ finish using Al_2O_3 powder and then etched by the etchant mentioned above. The fractured surfaces were also observed after tensile testing of each specimen.

In order to understand the effect of hydrogen on microstructure, both the samples were separately hydrogen charged for 12 hour in 0.05 mol/l H_2SO_4 solution at a current density of 10 mA/cm^2 . After hydrogen charging, the samples were slightly polished up to 600 grit level and then etched to reveal the microstructure and observed again in SEM. Similarly, several immersion tested samples were also observed in SEM to study the corrosion effect on microstructure.

3.10 EPMA Study

The local compositions in the carbon alloyed intermetallics were analyzed using a JEOL electron probe micro-analyzer (JXA-8600MX). The analysis was performed on many points at each specimen surface. As the Al was not mounted in the same holder as the Fe and C standards, quantitative analyses could not be performed. Only qualitative analysis was performed in order to confirm the nature of the precipitates observed.

Chapter 4

Results and Discussions

The results obtained in the present study are presented and simultaneously discussed in the present chapter.

4.1 Microstructural Study

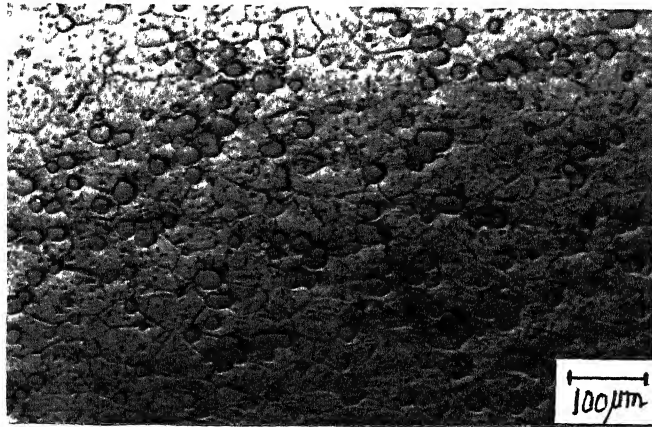
The microstructures of the alloys were studied by optical and scanning electron microscopy. The microstructural study of the alloys ESR56 and ESR63 revealed that they possessed recrystallized grains. This is expected as the thermomechanical processing of the alloys was performed at a high temperature where dynamic recrystallization had taken place [9]. The carbide particles were uniformly distributed throughout the matrix of iron aluminide. The carbide particles were generally spherical in shape as seen in optical micrographs of Figures 8(a) and 8(b). These microstructures were taken from the rolling plane. The microstructures in the transverse plane were similar to that in the rolling plane as the alloys were in the recrystallized condition. It should also be noted that the fraction of these spherical-shaped carbide particles is more in the case of ESR63 (Figure 8(b)) compared to ESR56 (Figure 8(a)).

The microstructures were analyzed for obtaining information on the spherical carbide particle distribution (the carbide particle size and its surface area per unit volume). For this purpose, five photographs of each sample were taken at different places at a magnification of 100X. The outline of the carbide particles in each photograph was traced on to a meshed tracing paper. The area of each particle was calculated by counting every small square inside the surrounding lines. The square was counted one when half of area of square was inside the line and zero when half and more of its area was outside. The area of

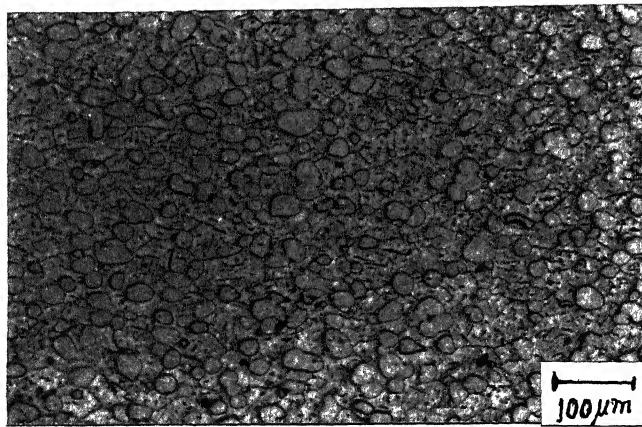
carbide particles was summed and divided by the total photograph area to obtain the area fraction of second phase carbide particles. This was equal to the volume fraction of the carbide particles and is reported in Table 6. In order to calculate the average mean diameter of carbide particles, the diameter of each particle was determined in a certain longitudinal direction. Then the diameters were arranged in different ranges and number of particles were counted for each range. The average diameter (weighted mean) was calculated by multiplying each range's representative diameter to number of particles in that range and sum up all the values obtained and then dividing it by total number of particles in that photograph. The same procedure was also adopted for calculating the vertical diameter. The average of horizontal and vertical diameters was the average particle diameter from that photograph. The same procedure was adopted for all the ten photographs and average diameter of carbide particles of each sample (i.e. ESR56 and ESR63) was determined (Table 6). Assuming that the carbide particles were spherical in shapes, the number of particles per unit volume was calculated. With the known number of second phase carbide particles, the surface area of carbide particles per unit volume was estimated. The average carbide particle size (diameter), volume fraction and surface area per unit volume are presented in Table 6.

It is noticed that the size of the spherical carbide particles are approximately the same in both the specimens. As the ESR63 alloy possess a higher carbon content than ESR56, it possesses a higher spherical carbide volume fraction and surface area per volume of the spherical carbide particles. The large surface area of the carbide particles could influence trapping of hydrogen and therefore maybe expected to also affect hydrogen embrittlement of these alloys.

The microstructures were also studied by SEM and typical microstructures are provided in Figure 9(a) and 9(b). At higher magnifications in the SEM, it was noticed that were also some needle-shaped carbide precipitates. These kind of carbide precipitates have also been reported by Baligdad *et al.* In estimating the diameter and volume fraction of the carbide particles, these fine particles were neglected. Therefore, the data provided in Table 6 should be considered as only approximate and provides a qualitative picture of the distribution of the larger spherical carbide particles.



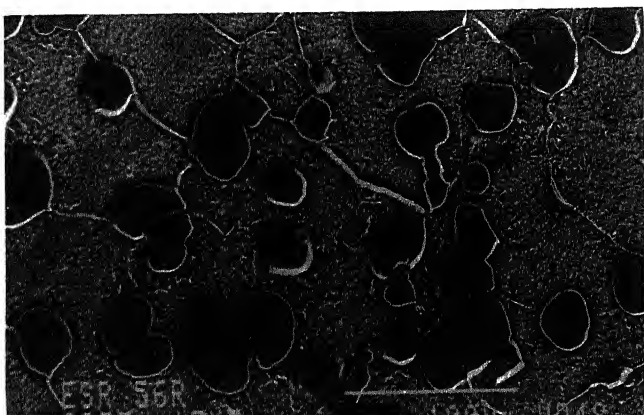
(a)



(b)

Mag.

Figure 8 Optical microstructure of (a) as received ESR56 sample, and (b) as received ESR63 sample



(a)



(b)

Figure 9 Scanning electron micrographs of (a) as received ESR56 sample, and (b) as received ESR63 sample

Table 6 : Size, volume fraction and surface area per unit volume of the carbide particles distributed in ESR56 and ESR63 samples

Sample	Diameter (in m) ($\times 10^{-5}$)	Volume fraction	Surface area/vol. (in m^2/m^3)
ESR56	3.7	0.15	2.4×10^4
ESR63	4.2	0.25	3.5×10^4

4.2 Composition Analysis

In order to determine the composition of the carbide particles, two techniques were utilized. These are discussed below.

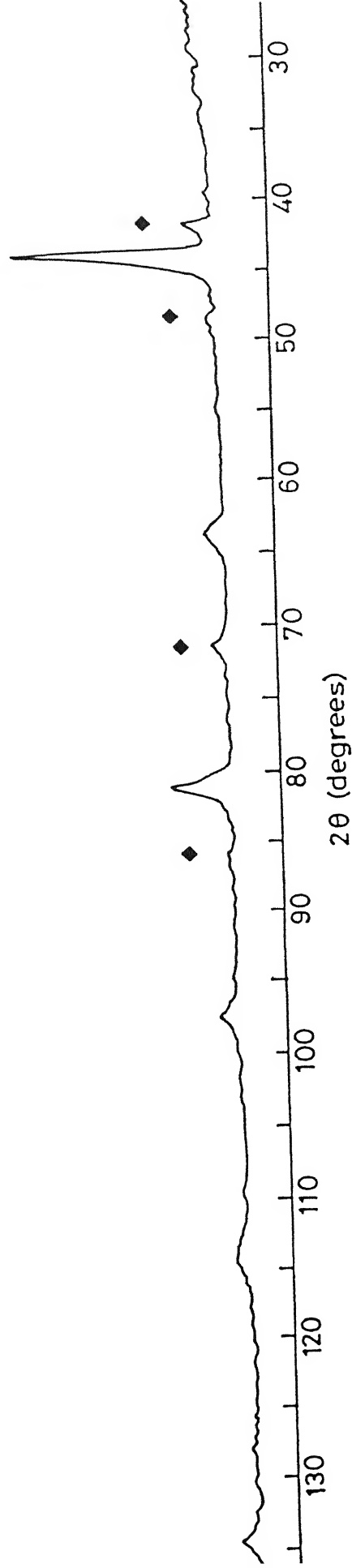
4.2.1 Electron Probe Microanalysis

The alloys were mounted in the electron probe microanalyzer and it was qualitatively determined that the second phase particles were composed of Fe, Al and C. However, the exact composition of the carbides could not be determined as there was no pure Al standard in the EMPA standard mount.

4.2.2 X-ray Diffraction

X-ray diffraction (XRD) patterns were obtained for both the samples ESR56 and ESR63 using $\text{CuK}\alpha$ ($\lambda = 0.15405 \text{ nm}$) radiation. The diffraction patterns for the samples ESR56 and ESR63 are presented in Figures 10(a) and 10(b), respectively. The patterns were analyzed and results are tabulated in Table 7 and Table 8. The major peaks belonged to Fe_3Al . After indexing the peaks of Fe_3Al (JCPDS file # 45-1203), the smaller peaks were indexed to the carbide Fe_3AlC (JCPDS file # 29-0044). It was assumed that the 100% carbide peak was the strongest carbide peak and the relative intensities for the carbide peaks were then obtained with reference to this peak (Tables 7 and 8). X-ray diffraction patterns confirmed that the presence of carbon leads to the formation of Fe_3AlC precipitates in the matrix. This Fe_3AlC phase has a FCC crystal structure with Al atoms occupying the corners of the cube, Fe atoms at the face centers and the carbon atom at the body center position (i.e. the octahedral void at $\frac{1}{2}, \frac{1}{2}, \frac{1}{2}$) [45]. The published lattice parameter of the structure is 0.377 nm and the indexing of carbide peaks in the pattern provided a lattice parameter of 0.374 nm. The slight mismatch of the calculated lattice parameter with the published lattice parameter could be due to the relatively small number of data points (i.e. d_{hkl} values) utilized to calculate the lattice parameter. In summary, the XRD analysis confirmed the presence of carbide particles and their composition.

◆ Fe_3AlC



◆ Fe_3AlC

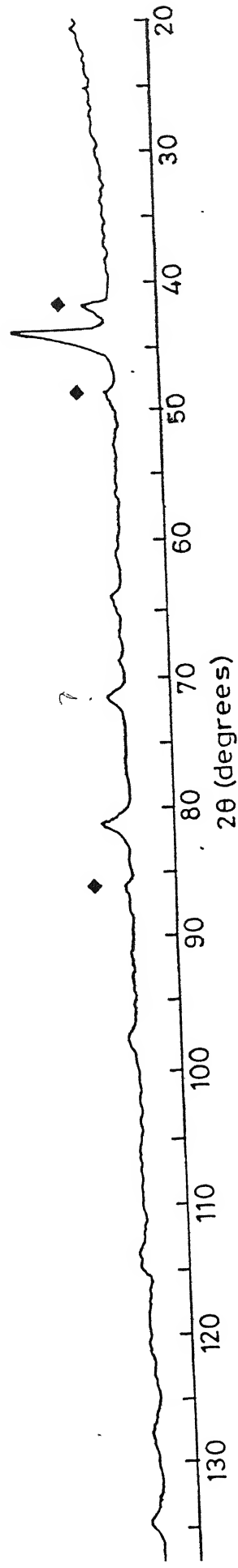


Figure 10 X-ray diffraction pattern of (a) ESR56 sample, and (b) ESR63 sample, using $\text{CuK}\alpha$ ($\lambda = 0.15405 \text{ nm}$) radiation

Table 7: Analysis the X-ray diffractogram of ESR63 using CuK_α ($\lambda = 0.15405 \text{ nm}$) radiation

Line#	$2\theta_{\text{obs}}$	$2\theta_{\text{theo}}$	hkl_{obs}	hkl_{theo}	d_{hkl} (\AA) _{obs}	d_{hkl} (\AA) _{theo}	$(I/I_0)\%_{\text{obs}}$	$(I/I_0)\%_{\text{theo}}$	Phase
1	41.8	41.44	111	111	2.16	2.17	100	100	Fe_3AlC
2	44.2	44.18	220	220	2.04	2.04	100	100	Fe_3Al
3	48.3	48.23	200	200	1.88	1.88	64.7	47	Fe_3AlC
4	64.2	64.25	400	400	1.44	1.44	10	12	Fe_3Al
5	81.3	81.28	422	422	1.18	1.18	39.4	19	Fe_3Al
6	86.2	85.32	311	311	1.12	1.13	52.9	13	Fe_3AlC

Table8: Analysis the X-ray diffractogram of ESR63 using CuK_α ($\lambda = 0.15405 \text{ nm}$) radiation

Line#	$2\theta_{\text{obs}}$	$2\theta_{\text{theo}}$	hkl_{obs}	hkl_{theo}	d_{hkl} (\AA) _{obs}	d_{hkl} (\AA) _{theo}	$(I/I_0)\%_{\text{obs}}$	$(I/I_0)\%_{\text{theo}}$	Phase
1	41.5	41.44	111	111	2.17	2.17	100	100	Fe_3AlC
2	44	44.18	220	220	2.04	2.04	100	100	Fe_3Al
3	48.3	48.23	200	200	1.88	1.88	65.6	47	Fe_3AlC
4	64	64.25	400	400	1.45	1.44	18.03	12	Fe_3Al
5	81.1	81.28	422	422	1.18	1.18	37.7	19	Fe_3Al
6	85.5	85.32	411	411	1.13	1.13	56.25	13	Fe_3AlC

obs = observed
theo = theoretical

4.3 Hydrogen diffusivity

It has been well established that the poor ductility of iron aluminides at ambient temperatures is due to hydrogen embrittlement. Hydrogen is produced by the reaction of moisture with the iron aluminide and enters the lattice to cause embrittlement. Therefore, one of the important factor that needs to be understood is the diffusion of hydrogen in iron aluminides. With this in mind, the diffusivity of hydrogen in both the iron aluminides was determined by the technique of subsurface microhardness profiling after cathodic hydrogen charging [47,48]. This technique has been successfully utilized to determine room temperature hydrogen diffusivity in Al-Li alloys [47], several austenitic stainless steels [48], and stoichiometric Fe_3Al [28,48].

Therefore, the following paragraphs outline the determination of diffusivity of hydrogen in the carbon alloyed iron aluminides used in the present study by this technique .

The procedure used to obtain microhardness profiles has been explained in detail earlier in the Experimental Procedure section. It must be emphasized that the hardness values were taken from the matrix only and not from the carbide particles. The average microhardness values (from the six profiles obtained for each intermetallic) were used in plotting the microhardness profiles which are presented in Figure 11. The maximum scatter in the microhardness data was ± 20 MHv and generally it was much lower than this. The microhardness data for stoichiometric Fe_3Al is also presented in the same Figure 11. It should be noted that the bulk microhardness is higher in the carbon alloyed intermetallics when compared to the base intermetallic. Moreover, the higher the carbon content of the alloy, the higher is the bulk microhardness value. These is expected based on the strengthening offered by the carbides. In earlier study of Baligidad *et al* reported higher yield strengths and ultimate tensile strengths for carbon alloyed Fe_3Al . They attributed this increase in strength (compared to the binary intermetallic) to solid solution strengthening by the interstitial carbon, as well as precipitation hardening due to the presence of Fe_3AlC precipitates [13].

The variation of microhardness (MHv) from surface to bulk is due to the diffusing species (hydrogen) as there was no variation in microhardness with depth for the uncharged

specimens. Assuming $(C - C_b)$ to be proportional to increase in MHv over the bulk value viz. $(MHv - MHv_b)$, we obtain

$$(C - C_b)/(C_s - C_b) = (MHv - MHv_b)/(MHv_s - MHv_b)$$

where C_s is the surface concentration of diffusing species, C_b the bulk concentration of diffusing species and C the concentration of diffusing species at any point. The subscript b and s denote bulk and surface, respectively.

As the diffusion depth was much smaller compared to the specimen thickness, the problem was treated as unsteady diffusion through a semi-infinite flat specimen. It was further assumed the diffusion constant was constant in the entire diffusion zone and the surface concentration was not a function of time. In order to apply the standard solution to Fick's second law, for the above condition, it was also assumed that the diffusion occurred through a single phase. Although carbides particles were present in the material, this assumption is reasonable as hardness measurements were selectively obtained from the matrix and not on the carbides. The surface concentration is not a function of time and the standard diffusion equation to give

$$(MHv - MHv_b)/(MHv_s - MHv_b) = 1 - \text{erf}(z/2\sqrt{Dt}) = \text{erfc}(z/2\sqrt{Dt})$$

Now, as the assumption of constant surface concentration is not strictly valid because of slight variations in the specimen potential during cathodic hydrogen charging, C_s should be ideally eliminated from equation above. C_s can be eliminated and the diffusion coefficient was determined using equation by the following method [8]. A pair of points on the microhardness vs distance curve was chosen and the following parameter Y_{12} was obtained (for two given points 1 and 2) based on the following equation

$$\begin{aligned} Y_{12} &= (C_1 - C_b) * (C_s - C_b) / (C_2 - C_b) * (C_s - C_b) \\ &= (C_1 - C_b) / (C_2 - C_b) = \text{erfc}(z_1/2\sqrt{Dt}) / \text{erfc}(z_2/2\sqrt{Dt}) \\ &= (MHv_1 - MHv_b) / (MHv_2 - MHv_b) \end{aligned}$$

where MHV_1 , MHV_2 , MHV_b are the microhardness values and C_1 , C_2 and C_b are the hydrogen concentration at the locations 1, 2 and the bulk respectively. D is the only unknown parameter in the above equation for a given experiment. The above can be solved by using error function table and by trial and error solution. The actual diffusivities estimated from each sample are provided in the Table 9. The average hydrogen diffusivity in Fe_3Al [28,48] is also mentioned.

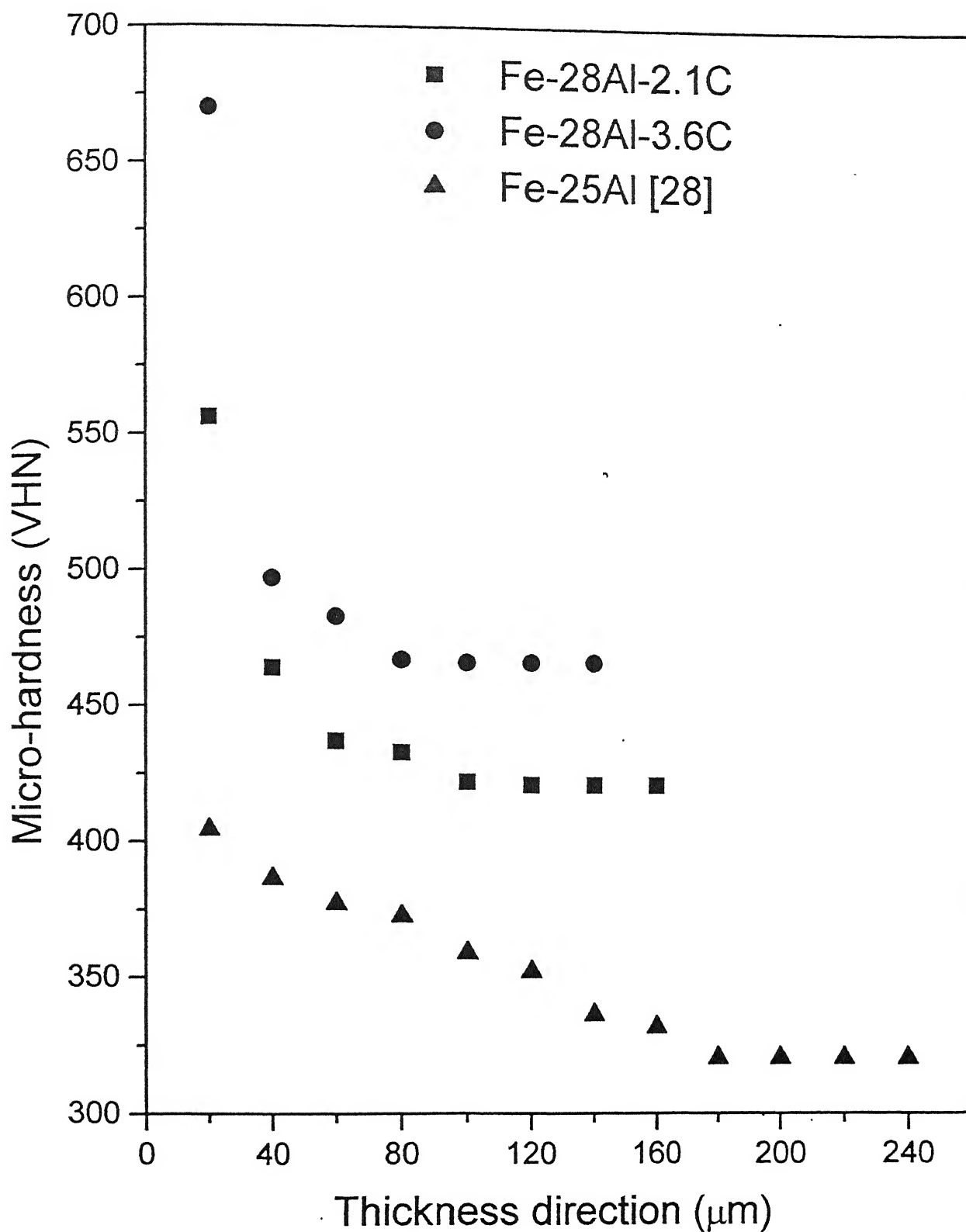


Figure 11 Microhardness profile of ESR56, ESR63 and Fe-25Al intermetallics, along the thickness direction after cathodic hydrogen charging for 12 hours at 10 mA/cm² in 0.05 mol/l H₂SO₄ solution

Table 9: Estimated diffusivity of hydrogen in the samples using 0.05 mol/l H_2SO_4 as electrolyte

Intermetallic	$D_{\text{H}} * 10^{-14} \text{ (m}^2/\text{s)}$	$D_{\text{H,avg}} \text{ (m}^2/\text{s)}$
Fe-25Al [28]	18.7, 16.7, 12.6, 11.3, 11.8, 12.4	$14.6 * 10^{-14}$
Fe-28.1%Al-2.1%C (ESR56)	0.45, 0.76, 1.57	$9.33 * 10^{-15}$
Fe-27.46%Al-3.66%C (ESR63)	0.43, 0.67, 1.48	$8.62 * 10^{-15}$

It is quite clear from Table 9 that hydrogen diffusivity in the carbon alloyed iron aluminide intermetallics was lower compared to that in the base intermetallic Fe-25Al. One possible reason for the same could be the irreversible trapping of the hydrogen atom by carbide particles (Fe_3AlC) in the matrix. Any diffusing species in the matrix can be trapped by the particles either reversibly or irreversibly [49]. Reversible trapping sites act as sink as well as source of the diffusing species. But, irreversible trapping sites act as only the sink of the diffusing species. It appears that the carbide particles act as irreversible traps for hydrogen atoms as the hydrogen diffusivity is lower in the carbon alloyed iron aluminide. It was also seen earlier that, as carbon content is higher in ESR63 than ESR56, the former has a higher carbide volume fraction. (Table 6). It is reasonable that a higher carbide volume fraction could offer more irreversible trapping sites and hence, lower hydrogen diffusivity. Therefore the lower hydrogen diffusivity observed in the ESR63 sample when compared to ESR56 sample must be related to a higher irreversible trapping of hydrogen in the matrix in the case of the former.

4.4 Room Temperature Aqueous Corrosion

In this section, the results of room temperature aqueous corrosion behavior, namely the potentiodynamic polarization behavior and corrosion rate studies, are discussed. The results of these studies are summarized in Table 10 and Table 11. All the potentials are with respect to saturated calomel electrode (SCE).

4.4.1 Potentiodynamic Polarization

The following discussion focuses attention on the potentiodynamic polarization behavior of both ESR 56 and ESR63 carbon-alloyed iron aluminide in the acidic medium ($\text{pH} = 1$) and buffer medium ($\text{pH} = 8.44$). The potentiodynamic polarization curves in the acidic medium, for ESR56 and ESR63, along with Fe-28Al intermetallic, are presented in the Figure 12, while the same in the buffer solution is presented in Figure 13. The various parameters from these plots are tabulated in Table 10. It is seen that both the alloys exhibit active-passive behavior in the acidic solution, in that there was a region where the current density was lowered on polarizing past the zero current potential. In the buffer solution, the polarization curves indicated that both the alloys ESR56 and ESR63 were passivated readily

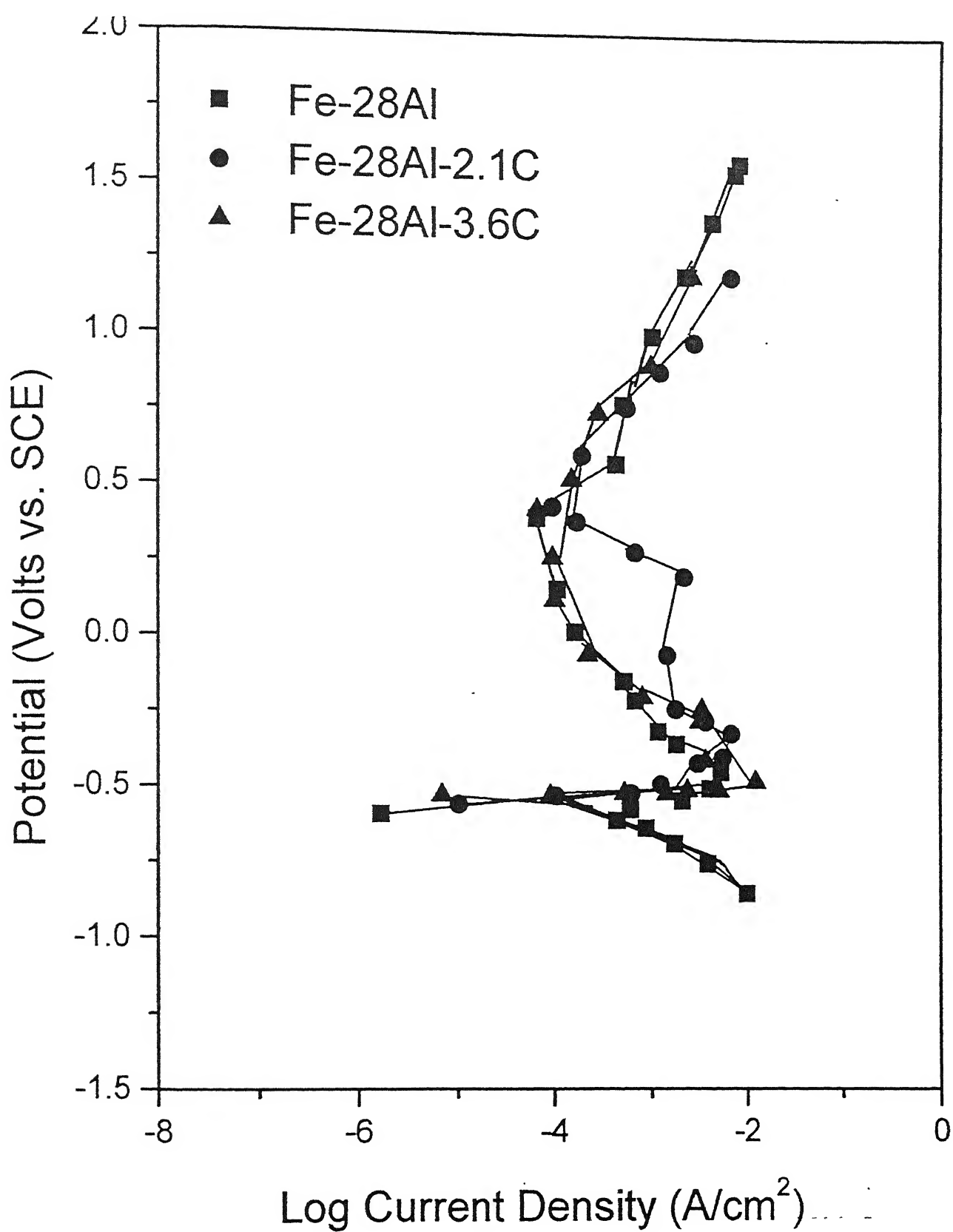


Figure 12 Potentiodynamic polarization behavior of ESR56, ESR63 intermetallics along with Fe-28Al intermetallic in 0.05mol/l H₂SO₄ solution

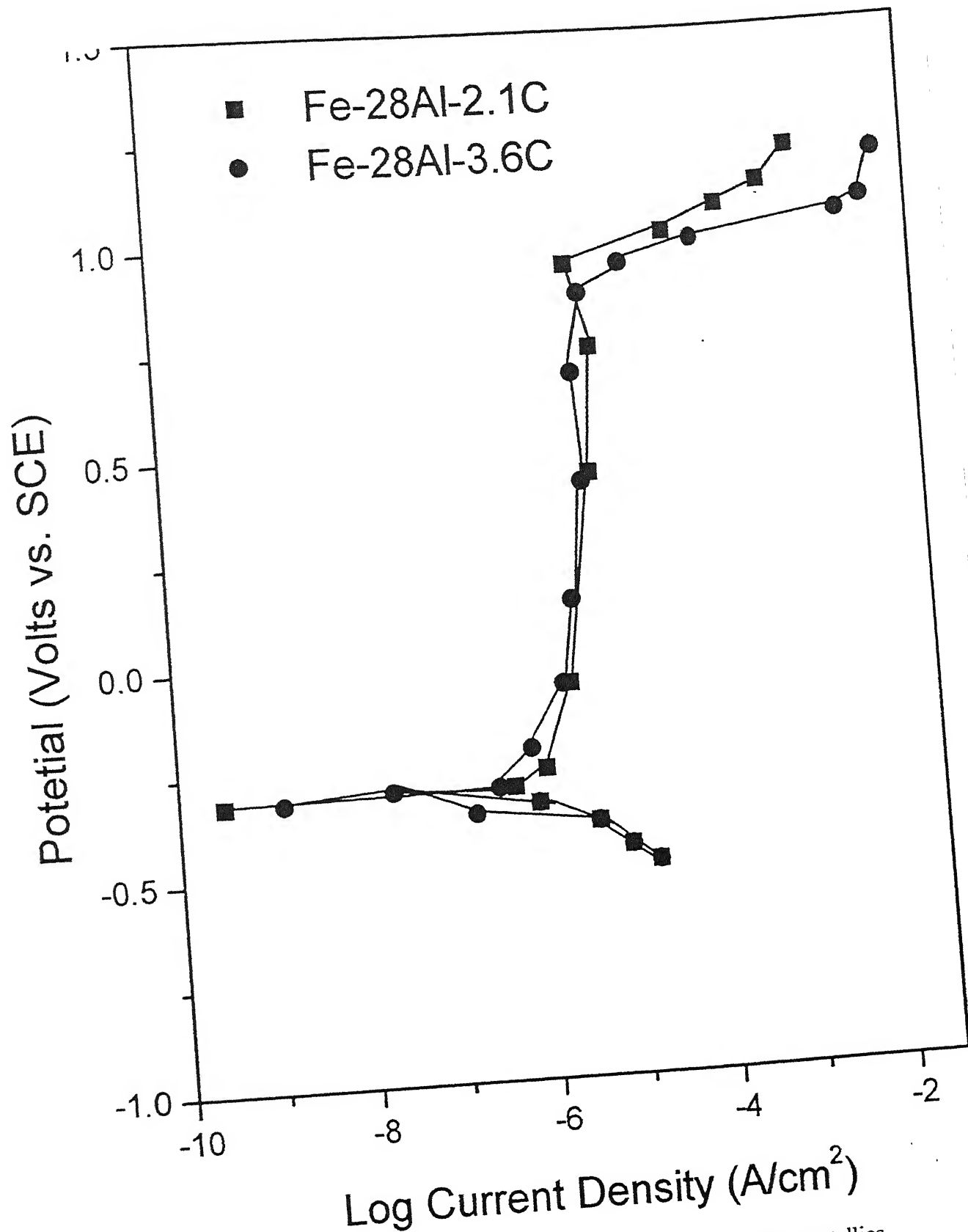


Figure 13 Potentiodynamic polarization behavior of ESR56, ESR63 intermetallics in buffer solution ($0.15N H_3BO_3 + 0.15N Na_2B_4O_7 \cdot 10H_2O$, $pH = 8.44$)

Table 10

Parameters determined from potentiodynamic polarization curves in buffer and 0.05 mol/l H_2SO_4 for the ESR56 and ESR63 samples

samples	β_a (V/dec.)	β_c (V/dec.)	R_p (Ω /dec.)	E_{corr} (V)	i_{corr} (A/cm ²)	E_{pp} (V)	$i_{critical}$ (A/cm ²)	E_{pass} (V)	i_{pass} (A/cm ²)	E_b (V)	Remarks
SR56 buffer	-0.04	0.077	57×10^3	-0.304	2×10^{-7}	-0.212	-	-0.21	1.3×10^{-6}	0.933	stable passivity
SR56 I_2SO_4	-0.199	0.263	32	-0.5371	1.54×10^{-5}	0.347	6.69×10^{-3}	0.36	8.3×10^{-5}	0.369	active- passive
SR63 buffer	-0.04	0.12	52×10^3	-0.2792	3.14×10^{-7}	-0.306	-	0.045	2.8×10^{-6}	0.885	stable passivity
SR63 I_2SO_4	-0.24	0.265	23	-0.5728	2.44×10^{-5}	-	9.86×10^{-3}	0.407	7.2×10^{-5}	0.408	active- passive

CENTRAL LIBRARY
I. I. T., KANPUR
A130851

Electrolyte used

$H_2SO_4 \rightarrow 0.05$ mol/lit.

Buffer $\rightarrow 0.15N$ Borric acid + 0.15N $Na_2B_4O_7 \cdot 10 H_2O$ (pH = 8.44)

on immersion. The passive current densities (i_{pass}) for both the alloys were lower in the buffer solution.

In the acidic solution, the critical current density for passivation (i_{crit}) was lower for ESR56. It appears, hence, that ESR56 (containing 2.1 at% C) was passivated more readily compared to ESR63 (containing 3.66 at% C). Moreover, the i_{crit} for the binary Fe-28Al is lower than that of ESR56, thereby indicating that with increasing C addition, the i_{crit} increases. As regards the passive region in the 0.05 mol/l H_2SO_4 solution, for the Fe-28Al intermetallic (without carbon addition), i_{pass} was equal to $7.4 \times 10^{-5} A/cm^2$ and E_{pass} was 0.372 V [15]. In the same solution, for ESR 56 and ESR63 i_{pass} were $8.31 \times 10^{-5} A/cm^2$ and $7.22 \times 10^{-5} A/cm^2$, and E_{pass} were 0.36 V and 0.4079 V, respectively. The above results indicate that there is only a marginal change in the polarization behavior of the two alloys in the acidic solution. The Fe-25Al intermetallic shows active behavior in the acidic medium [38]. It appears that passive layer readily form in the carbon alloyed iron aluminide compared to Fe-25Al intermetallic.

The corrosion rate can be obtained by Tafel and linear extrapolation methods. The corrosion rate in millimeters per year (mmpy) can be obtained from the polarization curve (where corrosion rate expressed in A/cm^2) by the following relation,

$$\text{Corrosion Rate (in mmpy)} = C.E.I_{corr} / d.A$$

- where,
- $C = 3.06 \times 10^5$ to obtain corrosion rate in mmpy.
 - E = Equivalent weight of the material in grams/mol.
 - I_{corr} = Corrosion current in Amp.
 - d = Density of the material in grams/ml.
 - A = Exposed cross section of the material in cm^2 .

For the carbon alloyed intermetallics, the values of E and d were taken as 21.7 gram/mol. and 6.72 g/cc, respectively. These are the values used generally for Fe-28Al intermetallic. The cross sectional area exposed for corrosion was 1 cm^2 . The corrosion current was obtained from the polarization curves presented in Figure 4.5. The corrosion rates thus obtained are 15.11 mmpy and 24.11 mmpy for ESR56 and ESR63, respectively, in the 0.05 mol/l H_2SO_4 solution. The results are comparable to the corrosion rates determined by the direct weight loss measurement in immersion testing, which will be discussed below. It should also be observed that ESR63 exhibited a higher corrosion rate compared to ESR56.

4.4.2 Corrosion Kinetics

The corrosion rates of the alloys were determined by constant immersion testing method. Two types of immersion tests were performed with the samples. One was relatively long term testing for a total of 8 days with weight losses being measured after every 12 hours, to see the long term corrosion effect on the samples. Another experiment was performed for a short duration of 24 hours and the weight losses measured after 30 minutes interval. The weight loss data in the same solution previously obtained by Babu [38] for Fe-25Al and Fe-28Al specimens have also been presented for comparison.

The results of the long term testing are discussed first. The weight loss data as a function of time (Table 11) was utilized to obtain the cumulative corrosion rate upto that point of time. The corrosion rate as a function of time is shown in Figure 14. The rates of corrosion were high after the first 12 hours for both the alloys. Thereafter, the corrosion rate decreased and after that it was almost constant in the last few days of the experiment. A similar behaviour was also observed for Fe-25Al [38]. The rate of corrosion was quite high in the initial stage of the experiment. In order to understand this behavior, short term immersion tests were carried out for a total duration of 24 hours and the weight loss was measured every 30 minutes. The results are shown in the Figure 15. The corrosion rate increase initially and after attaining a peak value at about 2 hours, decreased continuously. Interestingly, the Fe-28Al specimen tested by Babu [38] also exhibited a similar behaviour in that the corrosion rate was maximum after a certain period of immersion and then decreased with time. It is important to note that the corrosion rate values for the specimens in the present study are comparable to that for Fe-25Al and Fe-28Al. The possible explanation of this kind of behavior (i.e. higher rate of corrosion in the initial stages) could be due to selective dissolution. Selective dissolution could imply either selective dissolution of one phase or selective dissolution from some selective locations in the material. Once stable equilibrium conditions are attained, the rate of corrosion would then decrease. The decrease in corrosion rate in the final stages indicates that the alloys must have attained the equilibrium surface layer in the solution. It also appears that the presence of carbide-metal interfaces accelerates this process, which is indicated by the shorter times it took to achieve the maximum in corrosion rate for the carbon-alloyed intermetallics. Another possible reason for the

Table : 11 Corrosion rate of the samples at room temperature in 0.05M H₂SO₄ solution

Exposure time (days)	Weight loss /Area (gm/cm ²)		Corrosion rate (mmpy)	
	ESR56	ESR63	ESR56	ESR63
0.5	0.023	0.023	26.09	19.94
1.0	0.028	0.037	15.47	14.62
1.5	0.028	0.035	10.49	9.99
2.0	0.038	0.049	10.45	10.55
2.5	0.040	0.050	8.82	8.68
3.0	0.042	0.051	7.55	7.38
3.5	0.042	0.052	6.55	6.44
4.0	0.042	0.052	5.79	5.69
4.5	0.031	0.053	5.23	5.10
5.0	0.045	0.058	4.96	5.06
5.5	0.047	0.061	4.68	4.72
6.0	0.048	0.065	4.42	4.67
6.5	0.061	0.071	5.18	4.72
7.0	0.071	0.083	5.58	5.14
7.5	0.073	0.085	5.02	4.62
8.0	0.075	0.086	4.84	4.39

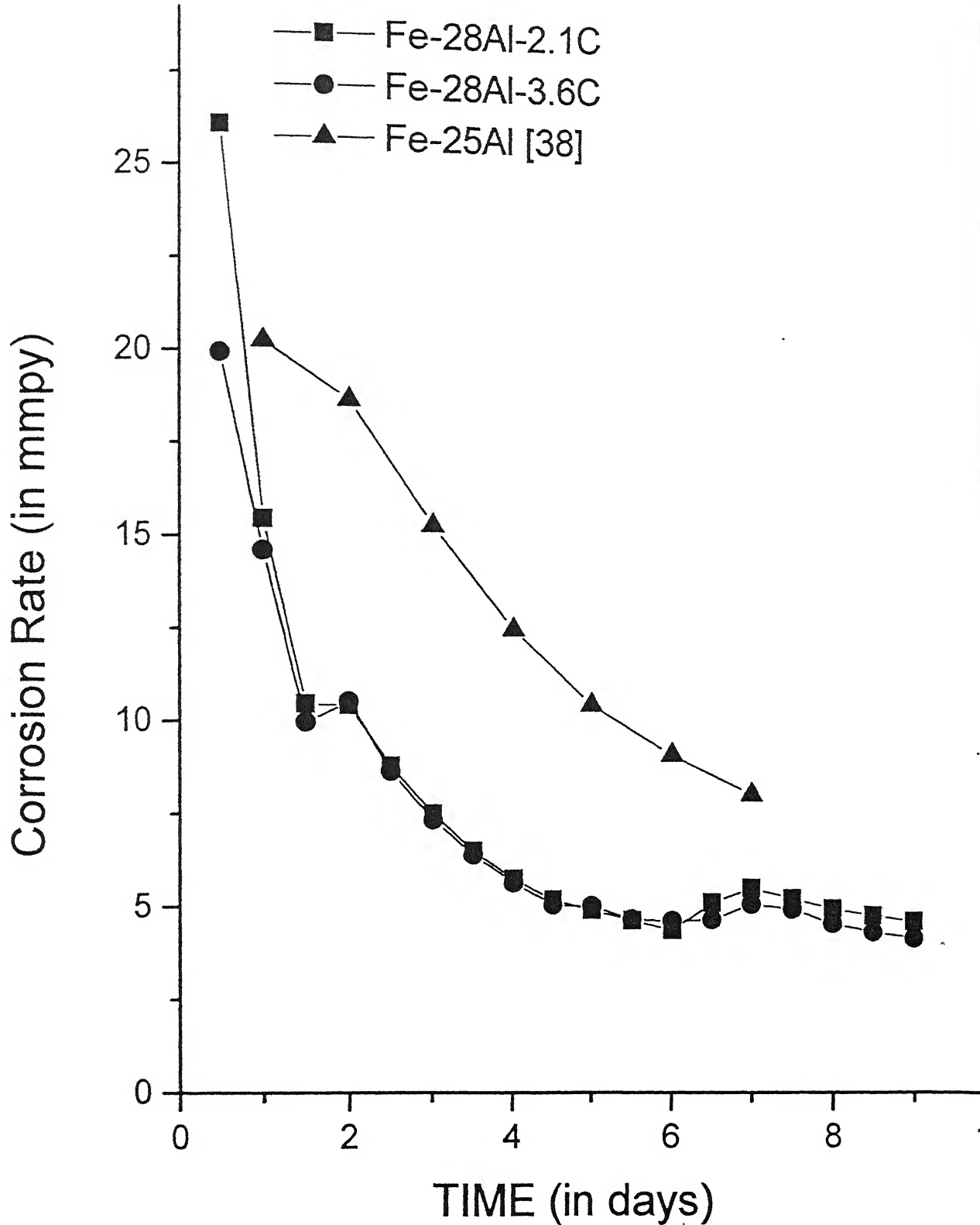


Figure 14 Long term immersion testing of ESR56 and ESR63 samples for 8days in 0.05 mol/l H_2SO_4 solution

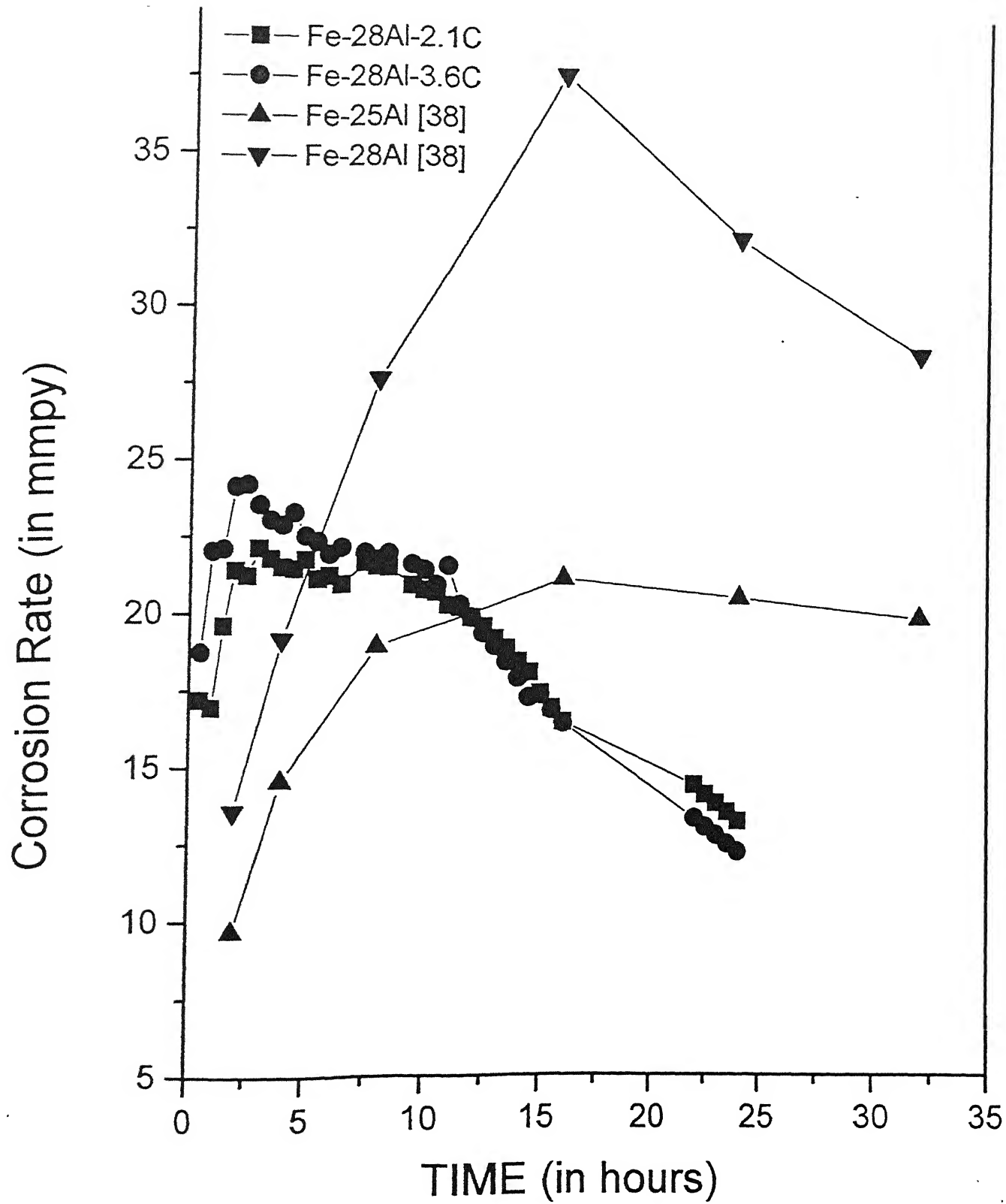
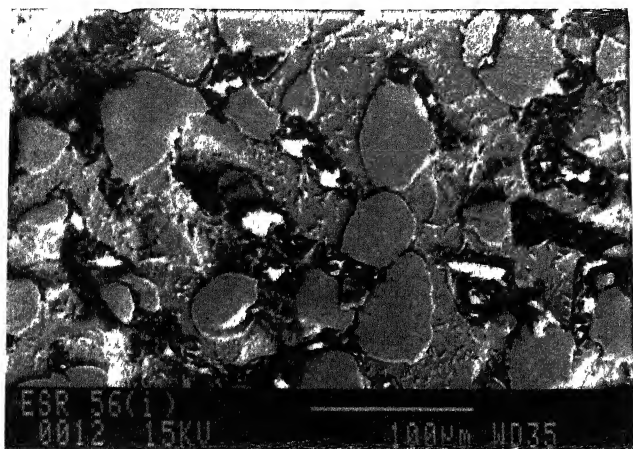
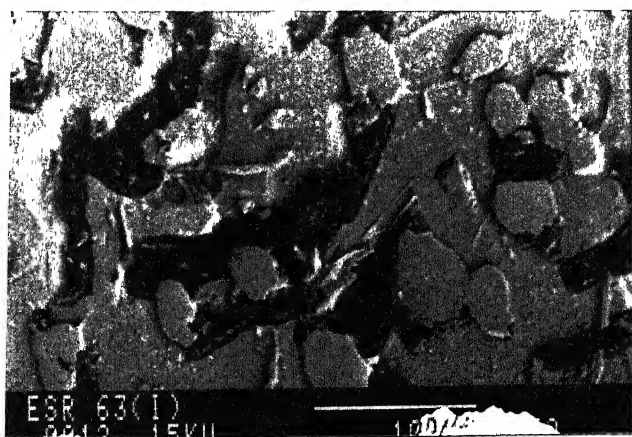


Figure 15 Short term immersion testing of ESR56 and ESR63 samples for 24 hours in 0.05 mol/l H_2SO_4 solution



(a)

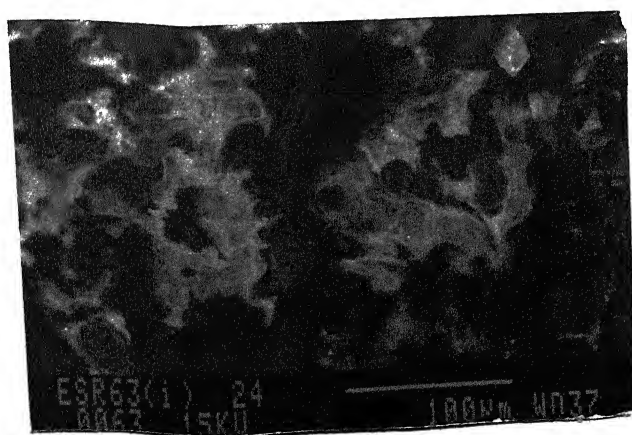


(b)

Figure 16 SEM micrographs of (a) ESR56 alloy and (b) ESR63 alloy, after immersed in 0.05 mol/l H_2SO_4 solution for 2 hours



(a)



(b)

Figure 17 SEM micrographs of (a) ESR56 alloy and (b) ESR63 alloy, after immersed in 0.05 mol/l H_2SO_4 solution for 24 hours

decreasing corrosion rate would be due to decreasing corrodability of the solution with time. This seems unlikely in the present case as the solution used for testing was relatively strong. The surfaces of the immersed samples were observed in the SEM after 2 hours and 24 hours of exposure in the 0.05 mol/l H_2SO_4 solution. From the SEM photographs (Figures 16 and Figure 17), it is clear that the particle-matrix interfaces were the selective locations for corrosion. In some cases, this lead to the formation of corrosion pits at the interfaces. The carbide particles were not corroded with respect to the matrix. This is reasonable as carbon is a relatively noble material as the carbide consists of a significant amount of carbon. The enhanced selective corrosion at the carbide-matrix interfaces could be due to distance effect in galvanic corrosion. The matrix is the anode and carbide the cathode in the galvanic cell. Therefore, during exposure in the solution, the matrix preferentially corrodes specially at the carbide-matrix interfaces. Interestingly, these selective dissolution sites can act like pits with time and these are potential sites for crack initiation by environmental degradation mechanism (stress corrosion cracking, hydrogen embrittlement).

4.5 Mechanical Properties

Tensile tests were conducted for the samples ESR56 and ESR63 in both the rolling direction as well as transverse directions. Duplicate tensile tests were performed for both the samples after hydrogen charging plus baking treatment. The tensile test results are presented in the Table 12. Interestingly, for both the samples, significant differences in the tensile properties like UTS and total strain were not observed for testing in the rolling and transverse directions. This was anticipated from the microstructural study, as both the samples showed similar equiaxed grains in the microstructures (Figures 8(a) and 8(b)).

For the reference samples, which were never charged with hydrogen, the stress-strain curves indicated yield stresses only in some cases. In the uncharged samples, very little plastic strains (ϵ_p) were observed. In the hydrogen charged+baked samples, yield stresses were generally not obtained. In all the cases the samples fractured in the linear portion in the stress-strain curve. In both these cases, hardly any ductility was observed in any sample. The possible reason could be that the Fe_3AlC phase is a hard and brittle phase, and its presence may be normally expected to embrittle the Fe_3Al -based alloys [9]. In the stress vs strain curve for all the samples, stress increased steadily (linearly) with the increase in strain upto

Table 12 Room temperature mechanical properties of hydrogen charged + baked (hb) and uncharged (u) intermetallics. *R* denotes guage length parallel to rolling direction while *T* denotes guage parallel to transverse direction.

Specimens	Y.S.(Mpa)	U.T.S. (Mpa)	ϵ_p ($\times 10^{-3}$)	ϵ_f ($\times 10^{-3}$)	H.E. index based on U.T.S. (%)	H.E. index based on ϵ_f (%)
ESR56R(u)	188	335	3.11	21.18	27.27	38.38
ESR56R(hb)	----	427	----	29.31		
ESR56T(u)	198	400	3.05	22.58	2.35	34.27
ESR56T(hb)	----	409	----	30.32		
ESR63R(u)	375	573	2.96	35.97	-7.31	-4.36
ESR63R(hb)	----	531	----	34.4		
ESR63T(u)	----	400	----	25.3	22.1	20.11
ESR63T(hb)	----	488	----	30.4		

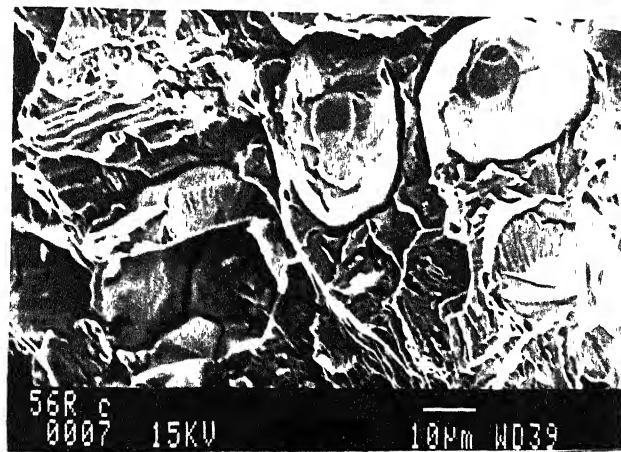


Figure 18 SEM fractograph of tensile sample after hydrogen charging+baking, showing interfaces are severely affected

the point of fracture. Therefore, the UTS corresponds the fracture stress (σ_f). ESR63 sample exhibited a higher fracture stress when compared to ESR56 sample.

After hydrogen charging+baking, virtually no plastic strain was obtained in any sample and this could be due to severe surface corrosion which occurred during hydrogen charging (Figure 18). This will be discussed more in detail later. The hydrogen embrittlement (H.E.) indexes for particular property are measured as the change in that property on hydrogen charging with respect to the initial property. In Table 12, the hydrogen embrittlement (H.E) indexes are presented for fracture stress (σ_f) and total strain (ϵ_f). It is clear that after hydrogen charging, ESR63, whose carbon content is higher than ESR56 alloy, was relatively more affected with respect to fracture stress and total strain.

Fractographic study also revealed that primary cracks were mainly initiated from the carbide particle interfaces. As the carbide content in ESR63 was higher, the corresponding number of carbide particle-matrix interfaces must also be higher and this could explain the ease of crack formation. In the ESR56 samples, after hydrogen charging the mechanical properties (fracture stress and total strain(ϵ_f)) were not significantly deteriorated. Therefore, it may that carbon content in ESR56 may be nearer to the optimum amount in order to tackle the hydrogen embrittlement effect at room temperature by irreversibly trapping hydrogen.

4.6 Fractography study

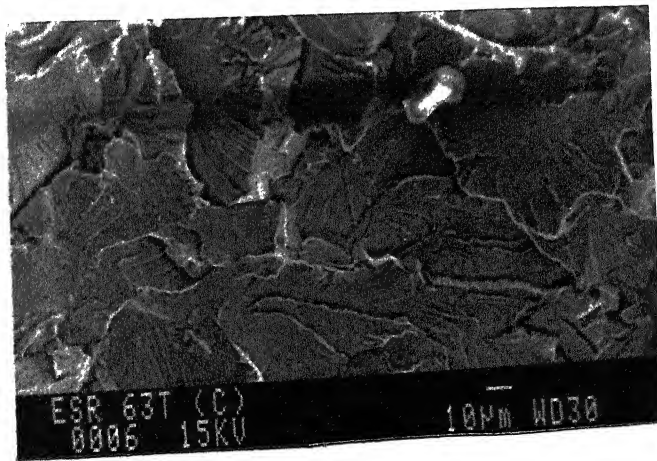
The fracture characteristic of all the tensile specimens were observed under scanning electron microscope. Fracture surfaces show mainly cleavage-type fracture in most of the cases. A typical example is shown in Figure 19b. This is typical for iron aluminides [37]. In the uncharged ESR56R and ESR63R samples, a mixed mode (ductile-brittle) fracture was observed (Figure 20b). These samples also exhibited a small ductility in the tensile curve (Table 12).

It was also noticed that the carbide particles were related to failure. A typical feature noticed in Figure 20a, where cracks are seen to originate from the carbide-matrix interfaces and propagate in the matrix. The absence of ductility even in the reference specimens could be due to this.

In some hydrogen charged samples, delamination at the carbide-matrix interface could be observed (Figure 19a). Notice that some carbide particles are also cracked in this

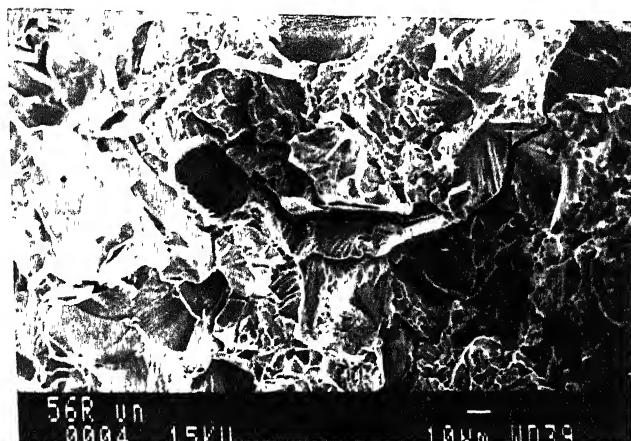


(a)

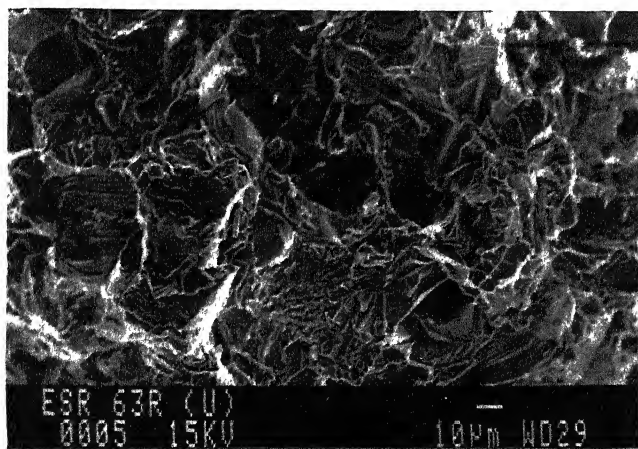


(b)

Figure 19 SEM fractograph of tensile sample after hydrogen charging+baking, (a) showing delamination effect at the carbide-matrix interfaces, and (b) showing mainly cleavage type of fracture surface



(a)



(b)

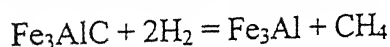
Figure 20 SEM fractograph of tensile sample with out hydrogen charging.
 (a) showing fracture mainly originated from the carbide-matrix interfaces,
 and (b) showing mixed mode (ductile-brittle) fracture surface

figure and that the fracture is cleavage-type failure. Primarily cracks were initiated near the surface as hydrogen was able to penetrate upto a short distance in the charged specimen. This is also confirmed from the microhardness profile (shown in Figure 11) of the hydrogen charged samples. In the hydrogen charged specimens, several cleavage facets are observed, indicative of very brittle type failure. The fractographic study indicated that the very low ductility, specially in the hydrogen charged specimens, could be attributed to the effect of hydrogen embrittlement as hydrogen was irreversibly trapped at the carbide-matrix interfaces. Moreover, the reference uncharged specimens did not exhibit much ductility since carbide particles possibly could be cracked due to application of tensile load, with the cracks mainly originating from the carbide-matrix interfaces.

4.7 Effect of Hydrogen Charging on Microstructure

The characteristic features of the sample surface after hydrogen charging are presented in the following paragraphs. The hydrogen was charged electrochemically in each specimen. The specimen acted as cathode, with respect to the platinum anode in the electrochemical cell containing 0.05 mol/l H_2SO_4 solution. The following observations were recorded in the hydrogen-charged samples (Figures 21a and 21b). First, there were several carbide precipitates that were cracked, with the cracks running through them (shown in Figure 21a). In several cases, pores could also be identified on the crack paths in the carbides (shown in Figure 21b). Secondly, there were several carbide particles where pores could be identified at the carbide-matrix interfaces. Thirdly, there were regions in the matrix where pores could also be identified. Finally, it was also seen that the matrix had corroded to some extent upon cathodic hydrogen charging.

The appearance of cracks in the carbide precipitates on hydrogen charging could result either due to a chemical reaction of the carbide with hydrogen or due to lattice dilation caused by the charging of hydrogen. The chemical reaction could be written as



for which the equilibrium constant K is written as,

$$K = ([a]_{Fe_3AlC} \times p_{CH_4}) / ([a]_{Fe_3Al} \times p_{H_2}^2)$$

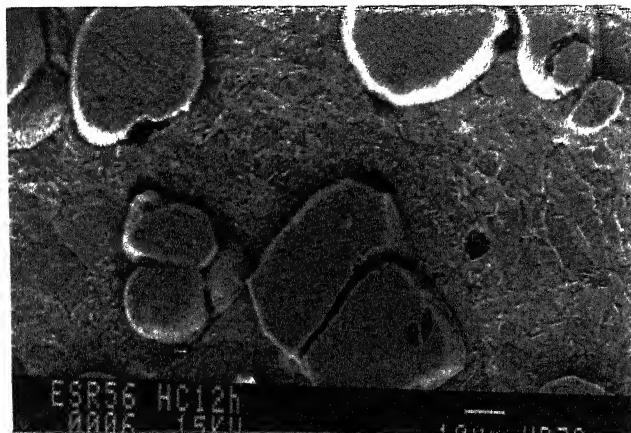
where a is activities of the species. As partial pressure of hydrogen increases, the forward reaction is favored at constant temperature. This would possibly lead to the more methane

formation by the above reaction at room temperature. In order to verify the reaction of the Fe_3AlC carbide precipitate with hydrogen, it was desirable to obtain the free energy of the reaction of the carbide with hydrogen. Unfortunately, the free energy for the formation of the carbide was not available and therefore the feasibility of the hydrogen reacting with the carbide could not be checked. However, there is an enormous literature available on the reaction of Fe_3C carbide with hydrogen and it is seen that it is favorable for hydrogen to react with this carbide in the process forming methane. This form of reaction is well catalogued and this is termed as hydrogen attack [15]. The reaction of the carbide with hydrogen is much faster at higher temperatures and this becomes a problem at higher temperatures. However, there is a feasibility for the reaction to occur even at room temperature based on free energy considerations and therefore, it is reasonable to also assume that the Fe_3AlC carbide can react with hydrogen to form possibly methane gas. The high hydrogen pressure would be an added factor which enhances the feasibility of the reaction.

In case of gas formation, it is anticipated that the methane gas would have much larger volume compared to hydrogen and this will lead to the establishment of stresses within the carbide, thereby possibly cracking the same. The formation of pores at the carbide-matrix interface could be also related to the production of gases and it can be concluded based on the microstructural observations that the production of methane gas by reaction of the carbide with hydrogen could be likely. The formation of pores in the matrix locations could possibly be due to local hydrogen accumulation at the defects leading to hydrogen recombination and the likely formation of hydrogen bubbles.

The implications of the microstructural observation on the mechanical property would be briefly addressed. It was seen that there was no ductility in the hydrogen charged samples and this would imply that hydrogen was irreversibly trapped at the interfaces. However, it is also likely that with high pressure hydrogen charging, the carbide particles will react to form methane gas at the interface. As a consequence, there would be regions at the carbide-matrix interface that would be locally stressed more than the bulk of the material and this will add up with the external stress, thereby leading to cracks initiating from these locations. Therefore, it is anticipated that the fracture stresses in the case of charged specimens should be lower than the reference specimen. This behaviour obtains in the tensile testing (Table 12).

The cracking in the case of the intermetallic is cleavage-type and the cleavage fracture surface is characterized by the presence of river marks. These river marks lead one to the origin for the crack initiation and it was seen by SEM observation of the fracture surface that the beach marks in most of the cases on the fracture surfaces pointed to the carbide-matrix interfaces. Therefore, it is clear that the effect of hydrogen on the mechanical properties is related to the initiation of cracks at the regions where it locally accumulates, i.e. the carbide-matrix interfaces, either as hydrogen molecules or as the product of methane gas.



(a)



(b)

Figure 21 SEM micrographs of the carbon-alloyed intermetallic after hydrogen charging for 12 hours at 10 mA/cm² in 0.05 mol/l H₂SO₄ solution, showing (a) some cracked carbides particles, and (b) pore formation in the carbide particles

Chapter 5

Summary and Conclusions

The effect of carbon addition to the iron aluminides on several properties is addressed in this thesis. The salient conclusions of the present study are presented in the first half of this chapter and the suggested work for future in the latter half.

5.1 Conclusions

The following were the salient conclusions of the present study.

1. The microstructures of the carbon-alloyed iron aluminides confirmed the presence of Fe_3AlC precipitates. These precipitates were present in two shapes: spherical (which were relatively large) and needle-shaped (which were relatively small). The presence of this carbide was also validated by XRD study.
2. The diffusivities of hydrogen in both the samples were determined by the technique of subscale microhardness profiling after cathodic hydrogen charging. The estimated hydrogen diffusivities (in m^2/s) were 9.33×10^{-15} for ESR56 and 8.62×10^{-15} for ESR63. The lower hydrogen diffusivity in ESR63 should be related to the larger volume fraction of carbides in the alloy. This indirectly indicated that carbide particles (Fe_3AlC) act as the irreversible hydrogen trapping sites and lower hydrogen diffusivity. The location where hydrogen is irreversibly trapped, is not exactly known, but most likely at the carbide-matrix interfaces.
3. Electrochemical polarization studies indicated that the alloys exhibit active-passive behaviour in acidic solution (0.05 mol/l H_2SO_4) whereas they exhibit stable passivity in (pH=8.4) buffer solution (0.15N Boric acid + 0.15 N $\text{Na}_2\text{B}_4\text{O}_7 \cdot 10\text{H}_2\text{O}$).

4. Corrosion kinetics was studied by weight loss method. In the long-term experiment of eight days, the corrosion rates were higher in after the first 12 hours for both the samples (ESR56 and ESR63). In the short-term experiment of 24 hours, the rate of corrosion was higher in the initial stages of experiment. The enhanced corrosion rates in the initial periods of immersion were due to the selective dissolution of the matrix. Once the equilibrium conditions were attained, the corrosion rate was decreased. Microstructural observations indicated that the carbide-matrix interfaces were severely corroded, which has been explained based on distance effect in galvanic corrosion.
5. As regards the mechanical properties, the specimens exhibited poor ductilities both in the uncharged and charged+baked conditions. The deterioration in mechanical properties on hydrogen charging was relatively more in the case of ESR63 compared to ESR56. This has been related to initiation of fracture at the carbide-matrix interfaces. Both the alloys exhibited brittle cleavage type fracture after hydrogen charging+baking. In cases where some ductility was observed, the fracture was mixed mode type.
6. The effect of hydrogen charging on microstructure was also studied separately by scanning electron microscopy. Several carbide particles were cracked after charging and moreover, the presence of cracks in the carbides could be seen. There were several carbide particles where pores could be identified at the carbide-matrix interfaces. Finally, it was also observed that the matrix had corroded to some extent upon cathodic hydrogen charging. The cracking of the carbide precipitates on hydrogen charging could result either due to a chemical reaction of the carbide with hydrogen or due to lattice dilation caused by the solution of hydrogen. Based on the microstructural study, it is more likely that the deleterious effect of hydrogen charging+baking on the mechanical properties is related to the initiation of cracks at the regions, i.e. the carbide-matrix interfaces, where it locally accumulates.

5.2 Suggestions for Future Work

Some of the additional works, which need to be undertaken in order to resolve some of the issues raised in this thesis, are:

1. The chemical reaction between carbide particle (Fe_3AlC) and hydrogen at room temperature should be studied in greater detail.
2. The potentiodynamic polarization studies should be conducted in solutions containing ions (that are capable of passivating the surface like phosphate or chromate ions and also that are capable of destabilizing the film on the surface like chloride ions) in order to understand hydrogen liberation under these conditions and the nature of the passive film.
3. Corrosion rate measurements by the weight loss technique should be conducted complementing the polarization studies.
4. The high temperature oxidation behavior of the carbon-alloyed intermetallics should be studied to validate its potential as candidate high temperature materials.
5. The microstructure of the carbon-alloyed intermetallics should be varied utilizing thermomechanical treatments. It is anticipated that proper control of the microstructure can result in a significant ductility increase as the present study has validated the beneficial role of the second phase carbide particles in trapping hydrogen (and thereby delaying hydrogen embrittlement).
6. The optimum carbon percentage in carbon-alloyed iron aluminide to obtain optimum room temperature as well as high temperature properties should be worked out based on a thorough study.

References

- [1] N.S.Stoloff, "Ordered alloys-physical metallurgy and structural applications", *International Metal Review*, **29**, 123-135 (1984)
- [2] C.T.Liu, J.O.Stiegler and F.H.Froes, "Ordered Intermetallics", *Metal Handbook 10 th ed.*, ASM, Materials Park, USA, Vol. 2, 913-942 (1990)
- [3] C.T.Liu and K.S.Kumar, "Ordered Intermetallic alloys, Part 1, Nickel and Iron aluminides", *J.Metals*. **45**, 38-44 (1993)
- [4] C.T.Liu, E.H.Lee and C.G.McKamey, "An environmental effect as the major cause room temperature embrittlement in FeAl", *Scripta Metall.* **23**, 875-880 (1996)
- [5] C.G.McKamey and C.T.Liu. "Chromium addition and environmental embrittlement in Fe₃Al", *Scripta Metall. Mater.* **24**, 2119-2122 (1990)
- [6] Zhang Zhonghua, Sun Yangshan, Liu Guijun, and Guo Jun, "Ductility improvement of Fe₃Al based alloys with surface coating", *Scripta Mater.*, **34**, 1071-1075 (1996)
- [7] R.Balasubramaniam, "On the role of chromium in minimizing room temperature hydrogen embrittlement in iron aluminides", *Scripta Mater.*, **34**, 127-133 (1996)
- [8] R.Balasubramaniam, "Alloy development to minimize room temperature hydrogen embrittlement in iron aluminides", *J.Alloys and Comp.*, 253-254 (1997)
- [9] R.G.Baligidad, U.Prakash, A.Radhakrishna and V.Ramakrishna Rao, "Effect of carbides on embrittlement of Fe₃Al based intermetallic alloys", *Scripta Mater.*, **36**, 667-671 (1997)
- [10] C.Sykes and J.Bampyfyld, "The physical properties of iron aluminium alloys", *J.Iron Steel Inst.*, **130**, 389-394 (1932)
- [11] C.T.Liu, C.G.McKamey and E.H.Lee, "Environmental effects on room temperature ductility and fracture mode in Fe₃Al", *Scripta Metall. Mater.*, **24**, 385-390 (1990)
- [12] Y.F.Zhu, C.T.Liu and C.H.Chen, "Direct evidence of hydrogen generation from the reaction of water with FeAl", *Scripta Mater.*, **35**, 1435-1439 (1996)

- [13] R.G.Baligidad, U.Prakash, A.Radhakrishna and V.Ramakrishna Rao, "Effect of carbon contents on high temperature tensile properties of Fe₃Al based intermetallic alloy", *Scripta Mater.*, **36**, 105-109 (1997)
- [14] H.K.Birnbaum, G.M.Bond and I.M.Robertson, "Effect of hydrogen on deformation and fracture process in high purity aluminium", *Acta Metall.*, **36**, 2193-2198 (1998)
- [15] D.A.Alven and N.S.Stoloff, *Scripta Metall.*, **34**, 1937 (1996)
- [16] N.S.Stoloff and D.J.Duquette, "Moisture and hydrogen induced embrittlement of iron aluminides", *J. Metals*, **45**, 30-35 (1993)
- [17] A.Agarwal, R.Balsubramaniam and S.Bhargava, "Effect of thermomechanical treatment on the room temperature mechanical behavior of iron aluminide", *Met. Mater. Trans.*, **27A**, 2985-2994 (1996)
- [18] D.G.Morris and M.Leboeuf, "The role of controlled recrystallization treatment on ductility of Fe₃Al alloys", *Acta. Metall. Mater.*, **42**, 1817-1823 (1994)
- [19] J.C.M.Li and T.Liu, "Crack nucleation in hydrogen embrittlement", *Scripta Metall. Mater.*, **27**, 1701-1705 (1992)
- [20] P. Banerjee and R. Balasubramaniam, "Hydrogen diffusivity in Fe-Al", *Bull. Mater. Sci.*, **20**, 713-717, (1997)
- [21] J.Volkl and G.Alefeld, "Diffusion of hydrogen in metals", *Topics in Applied Physics*, **28**, 321-344 (1978)
- [22] J.Volkl and G.Alefeld, "Diffusion in Solids, edited by A.S.Nowick and J.J.Burton", *Academic Press, New York, USA*, 231 (1975)
- [23] K.Kiuchi and R.B.McLellan, "The solubility and diffusivity of hydrogen in well-annealed and deformed iron", *Acta Metall.*, **31**, 961-984 (1983)
- [24] H.Chieu, L.Qiao and X.Mao, "Environmental assisted cracking of iron aluminide in 3.5% NaCl solution", *Scripta Mater.*, **34**, 963-969 (1996)
- [25] J.H.Zhu, S.B.Huang and X.J.Wan, *Scripta Metall.*, **32**, 1399 (1995)
- [26] P. Banerjee and R. Balasubramaniam, "Mechanical behavior of chromium and titanium alloyed iron aluminides with mischmetal addition", *Scripta Materialia*, **38**, 1143-1147, (1998)

- [27] C.G.McKamey, J.A.Horton and C.T.Liu, "Effect of chromium on room temperature ductility and fracture mode in Fe₃Al", *Scripta Metall.*, **22**, 1679-1681 (1988)
- [28] P.Banerjee. "Hydrogen behavior in Chromium and Titanium Alloyed iron aluminides", M.Tech Thesis, I.I.T., Kanpur, 1997.
- [29] M.A.Crimp and K.M.Vedula, "Effect of boron on the tensile properties of B2 FeAl", *Mat. Sci. Eng.*, **78**, 193-1999 (1986)
- [30] C.T.Liu and E.P.George, "Environmental embrittlement in boron free and boron doped FeAl alloys", *Scripta Metall. Mater.*, **24**, 1285-1290 (1990)
- [31] C.G.McKamey and D.H.Pierce, "Effect of recrystallization on room temperature tensile properties of an Fe₃Al based alloys", *Scripta Metall. Mater.*, **28**, 1173-1176 (1993)
- [32] D.Lin, A.Shan and D.Li, "Superplasticity in Fe₃Al-Ti alloy with large grains", *Scripta Metall. Mater.*, **31**, 1455-1460 (1994)
- [33] S.Yangshan, Y.Zhengjun, Z.Zhonghua and H.Haibo, "Mechanical properties of Fe₃Al based alloys with cerium addition", *Scripta Metall. Mater.*, **33**, 811 (1995)
- [34] C.G.McKamey, J.H.Devan, P.F.Tortorelli and V.K.Sikka, "A review of recent development in Fe₃Al based alloy", *J.Mater. Res.*, **6**, 1779-1786 (199)
- [35] R.Balasubramaniam, "On the role of chromium in minimizing room temperature hydrogen embrittlement in iron aluminides", *Scripta Mater.*, **34**, 127-133 (1996)
- [36] J.C.M.Li and T.Liu, "Crack nucleation in hydrogen embrittlement", *Scripta Metall. Mater.*, **27**, 1701-1705 (1992)
- [37] A.Agarwal and R.Balsubramaniam, "Fracture characteristics of alloyed iron aluminides", *Pract. Metallogr.*, **33**, 453-466 (1996)
- [38] N.Babu, "Room temperature aqueous corrosion and high temperature oxidation behavior of iron aluminides", M.Tech thesis, I.I.T., Kanpur, 1998
- [39] S.Mukherjee and R.Balasubramaniam, "Deciphering the potentiodynamic polarization curves of iron aluminides Fe₃Al and Fe₃Al+Cr", *Bull. Mater. Sci.*, **19**, 831-835 (1996)

- [40] A.Agarwal and R.Balasubramaniam, "Role of surface passive films on the hydrogen embrittlement of iron aluminides", *Bull. Mater. Sci.*, **19**, 91-102 (1996)
- [41] A.Agarwal, M.J.Akhtar and R.Balasubramaniam, "Effect of alloying on aqueous corrosion and mechanical behavior of iron aluminide Fe_3Al ", *J. Mat. Sci.*, **31**, 5207-5213 (1996)
- [42] V.K.sikka, "Processing and applications of iron aluminides", in *Processing, Properties and Applications of Iron aluminides*, eds. J.H.Schneibel and M.A.Crimp, TMS, Warrendable, USA, 3-18 (1994)
- [43] R.G.Baligidad, U.Prakas, V.Ramakrishna Rao, P.K.Rao and N.B.Ballal, "Electroslag remelting of Fe-28at% Al intermetallic alloy", *Iron and Steel making*, **21**, 324-331 (1994)
- [44] J.H.DeVan, "Resistance of iron aluminium alloys to oxidation at high temperature", in *Oxidation of High Temperature Intermetallics*, eds. TMS, Warrandable, USA, 107-115 (1989)
- [45] W.B.Pearson, "Handbook of lattice spacings and structures of metals".
- [46] C.Thakur and R.Balasubramaniam, "Determination of Hydrogen Diffusivity in Al-Li-Cu-Mg Alloys", *J. Mater. Sci. Lett.*, **15**, 1397-1399 (1996)
- [47] P.Kumar and R.Balasubramaniam, "Determination of hydrogen diffusivity in austenetic stainless steels by subscale microhardness profiling", *J. Alloys Compounds*, **255**, 130-134 (1997)
- [48] R.Balasubramaniam, "Determination of hydrogen diffusivity by subscale microhardness profiling", *J. Alloys and Compounds*, **293-295**, 279-281 (1999)
- [49] D.A.Jones, "Principles and prevention of corrosion", Maxell Macmillan International editions, 1992.
- [50] R. Balasubramaniam, "Environmental effects in iron aluminides", *Bull. Mater. Sci.*, **22**, 571-579 (1999)

130851

130851

Date Slip

This book is to be returned on the
date last stamped.

[illegible]

TH

MME/2000/M

S55e

A130851